Pergamon

A Constitutive Law for Bond Failure of Fully-grouted Cable Bolts Using a Modified Hoek Cell

A. J. HYETT†
W. F. BAWDEN†
G. R. MACSPORRAN‡
M. MOOSAVI†

A series of pull tests were performed using fully-grouted seven-wire strand cable, in which the confining pressure at the outside of the cement annulus was maintained constant using a modified Hoek cell. The bond strength was shown to increase with confining pressure. The associated radial displacements at the outside of the cement annulus were measured by two sets of diametrically opposed strain gauge arms located at the midpoint of the test section. The radial dilations decreased with confining pressure, so that at pressures corresponding to high bond strengths, less than 20 μm of radial deformation was generated after 50 mm of axial displacement. Observations under the scanning electron microscope revealed that the low dilations can be explained by the occurrence of an "unscrewing" failure mechanism along the majority of the test section.

The data were used to develop a frictional–dilational model for cable bolt failure in both graphical and mathematical form. The latter is amemable to implementation in numerical programs, and presents an opportunity to incorporate realistic cable bolt behaviour into numerical analyses.

From an operational perspective, the miniscule radial dilations induced by bond failure, which are responsible for the generation of radial pressure at the cable–grout interface and the development of frictional bond strength, explain the sensitivity of the bond strength to (i) the grout quality, (ii) the radial stiffness of the borehole wall and (iii) mining-induced destressing.

NOMENCLATURE

r_1 = inner radius of cement annulus, i.e. nominal radius of cable
r_2 = outer radius of grout annulus
r_c = radius for which radial fractures are open
L_e = embedment length
L_s = length of test section for which the grout flutes are sheared
L_f = free length of the cable between test and anchor sections
A_1 = aparent cable–grout interface contact area
p_1 = radial pressure at $r = r_1$
p_2 = radial pressure at $r = r_2$
p_c = radial pressure at $r = r_c$
σ_θ = tangential stress in the grout annulus
F_a = axial load on cable
Q = component of axial force related to untwisting the cable
u_a = axial displacement at exit point
u_{r1} = radial displacement at $r = r_1$
u_{r2} = radial displacement at $r = r_2$
u_{rc} = radial displacement at $r = r_c$
θ = twist of cable
k_j' = coefficients for cable bolt model

Grout properties

E_g = Young's modulus of the grout
v_g = Poisson's ratio of the grout
σ_c = compressive strength of the grout
ϕ_g = internal angle of friction for the grout
τ_0 = Mohr–Coulomb cohesion—intercept for the grout

Cable properties

E_c = axial Young's modulus of the cable
v_c = Poisson's ratio of the cable, i.e. contraction during axial pull
K_{rc} = radial stiffness of the cable
C = torsional rigidity of cable
l = pitch length of the cable
h_0 = height of grout flutes
α = angle of the pitch

Parameters for the cable–grout interface

ϕ_{gs} = friction angle between grout and steel
ϕ' = average coefficient of friction
v = dilation at cable–grout interface
v_{sp} = dilation due to splitting
v_0 = dilation due to splitting for $p_1 = 0$
K_0 = radial stiffness of the cable–grout interface after splitting for $p_1 = 0$

†Department of Mining Engineering, Queen's University, Kingston, Ontario, Canada K7L 3N6.
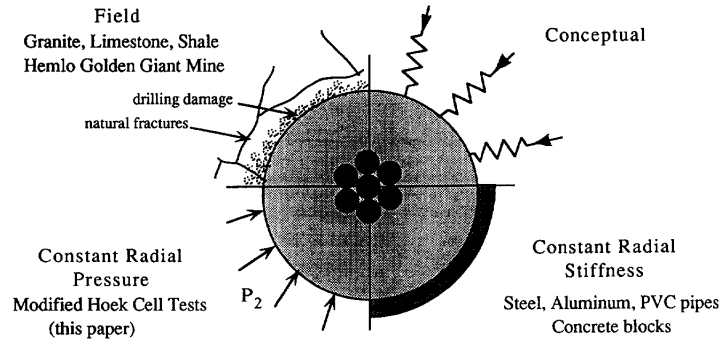‡Noranda Minerals Inc., GECO Division, Manatouwadge, Ontario, Canada.

Fig. 1. Boundary conditions to the cable–bolt system. In operational practise this consists of the borehole wall. In the laboratory, previous workers have used pipes and concrete blocks. In this research a constant radial pressure is applied and the dilations at the outside of the cement annulus were measured.

i = dilation angle of the cable–grout interface
k_1 = empirical constant describing pressure dependancy of radial displacement at the cable–grout interface

Rock properties

E_r = Young's modulus of rock
v_r = Poisson's ratio of rock
K_r = radial stiffness of the borehole wall

INTRODUCTION

The reinforcement of a rock mass using fully-grouted cable bolts falls into the general classification of a load transfer problem. As the basis of this problem, it is necessary to investigate the mechanics of load transfer between a single cable and the surrounding rock mass, in order to determine the combination of bond strength and embedment length required to most effectively reinforce the rock mass, without reaching the tensile strength of the cable (240–260 kN). During failure of cable-reinforced ground, both stress redistribution and a progressive deterioration of the rock mass quality may adversely affect both the bond strength and the embedment length available, potentially resulting in very poor cable bolt performance. Thus, any attempt to model the behaviour of a cable-reinforced rock mass must be based on a fully inter-active analysis in which the behaviour of the rock mass controls the bond strength of the cable bolt as well as vice versa.

Cable bolt research, both in the laboratory and field, has confirmed that the most prevalent mode of failure for a cement-grouted seven-wire strand involves frictional slip at the grout–cable interface. As the axial displacement (u_a) of the cable is increased, the frictional resistance (F_a) to pullout depends on the interaction between radial pressure (p_1) and radial dilation (u_{r1}) at the grout–cable interface, which themselves are controlled by factors such as:

    (i) the material properties and mechanical behaviour of the grout annulus
    (ii) the mechanical properties of the cable
    (iii) the radial confinement applied at the outside of the cement annulus.

Previous research has established that low water:cement (w:c) grouts are associated with high
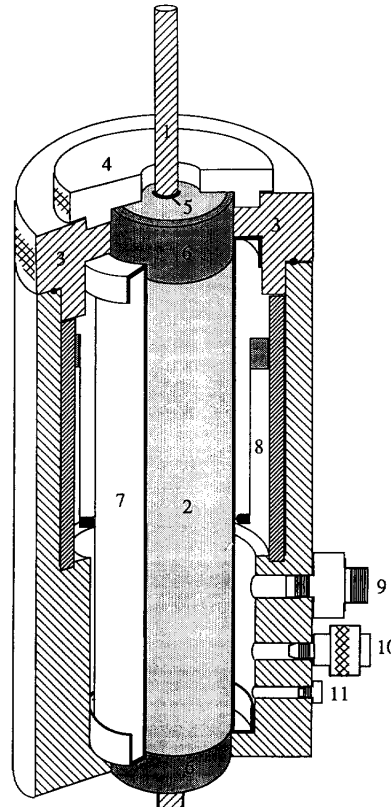
bond capacities [1, 2], and recent tests [3] have indicated a significant difference between pull test results conducted on grouted cables from different North American manufacturers. Concerning the latter, to the authors' knowledge, all laboratory cable pull tests have been conducted in either confining pipes [4–7], concrete blocks

Fig. 2. Cutaway section of the modified Hoek cell (MHC): (1) 15.2 mm (0.6″) seven-wire strand; (2) type 10 portland cement annulus; (3) pressure vessel endcap; (4) specimen endcap; (5) 15 mm PVC tube for debonding; (6) ABS pipe to support end of specimen and overcome end-effects; (7) neoprene bladder; (8) cantilever strain gauge arms; (9) high pressure electrical feedthrough; (10) high pressure fitting; (11) pressure transducer.
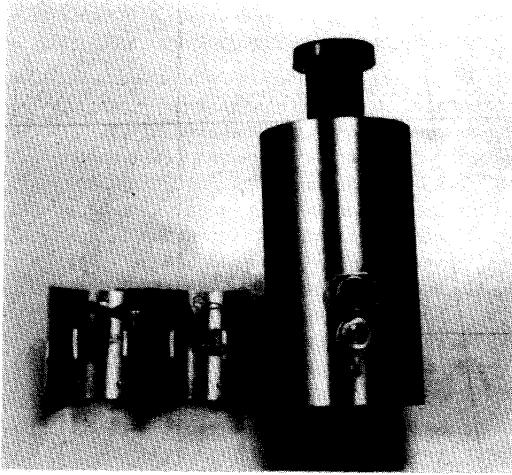
Fig. 3. Photograph of various components of the MHC.

[8, 9] or the *in situ* rock mass [10, 11]; namely under a constant radial stiffness boundary condition (Fig. 1). Reichert *et al.* [2] and Hyett *et al.* [6] demonstrated that a stiffer response and higher ultimate capacities were obtained for tests conducted in pipes with higher radial stiffness, and that, if the radial stiffness of the borehole wall was considered, these could be correlated with *in situ* tests. However, for all of these tests the confining pressure and dilation induced by bond failure were not monitored. This inhibited understanding of the mechanics of bond failure and the subsequent development of a realistic constitutive law.

In general, the boundary condition at the borehole wall can be conceptualized by the assumption of a spring with radial stiffness $K_r = dp_2/du_{r2}$, where dp_2 and du_{r2} are the changes in radial confining pressure and displacement, respectively. The applied stiffness K_r varies between zero for a cable bolt under constant radial pressure to infinity in the case where no change in radial dilation is allowed.

In the present test programme, all four test variables (F_a, u_a, p_2 and u_{r2}) were either controlled or monitored for a series of laboratory cable pull tests conducted in a triaxial Hoek cell. Ideally, the radial pressure and dilation (p_1 and u_{r1}) should have been measured/controlled at the cable–grout interface where slip is actually occurring and frictional resistance to pullout was mobilized. However, it would have been virtually impossible to determine the radial pressure and radial dilation generated there by direct instrumentation. As a practical compromise, a method was adopted whereby measurements were made at the outer surface of the grout annulus. Consequently, the deformation behaviour determined related not to that of

the cable–grout interface, but instead to that of the complete grouted cable bolt, which comprises the cable, grout annulus and the interface in between. Tests were conduced at a range of confining pressures expected to be representative of those that would be generated at the borehole wall during operational cable bolt bond failure.

EXPERIMENTAL PROCEDURE

Modified Hoek cell (MHC)

A triaxial cell, henceforth referred to as the modified Hoek cell (MHC), was designed, in which a series of cable pull tests were to be conducted under a condition of constant radial pressure (Fig. 2). The design was fundamentally similar to that described by Hoek and Franklin [12] which is widely used for the triaxial testing of intact rock cylinders. The principal design modifications that were introduced are listed below:

(i) the body of the cell was elongated to 285 mm to accomodate a 265 mm long rubber sealing sleeve or bladder of 50.8 mm (2") i.d.

(ii) the bottom of the cell was machined solid and the endcap omitted

(iii) an instrumentation collar was incorporated behind the rubber bladder on which were mounted two sets of diametrically opposed cantilever strain gauge arms oriented perpendicular to each other (Fig. 3), to monitor dilation at the middle of the sample

(iv) wires were led out through a high pressure feed-through within the cell body

(v) the cell was only designed to operate at pressures up to 20 MPa, so that the clearance gap could be designed with a lenient tolerance to facilitate removal of the test specimen after failure (see [12]).

The cell was proofed to 25 MPa, and a series of calibrations were conducted on steel and aluminium pipes with different o.d.s to account for the effect of the rubber bladder on the deformations measured by the strain gauge arms. The final design was robust enough to enable 40 tests to be conducted with a single bladder. The most persistent problem involved the removal of the failed specimen from the cell following a test.

Test sample preparation

Each pull test sample consisted of a 15.2 mm (0.6") seven-wire strand cable with a tensile strength of 240–260 kN or 24–26 tonnes (ASTM A416), grouted using a type 10 portland cement paste into two sections of pipe: a lower 2" Sch. 80 steel pipe 550 mm in length; and an upper 250 mm 2" Sch 80 PVC pipe (see [13] for further details). The former is used to anchor the test

Table 1. Properties of cement paste for different w:c ratios

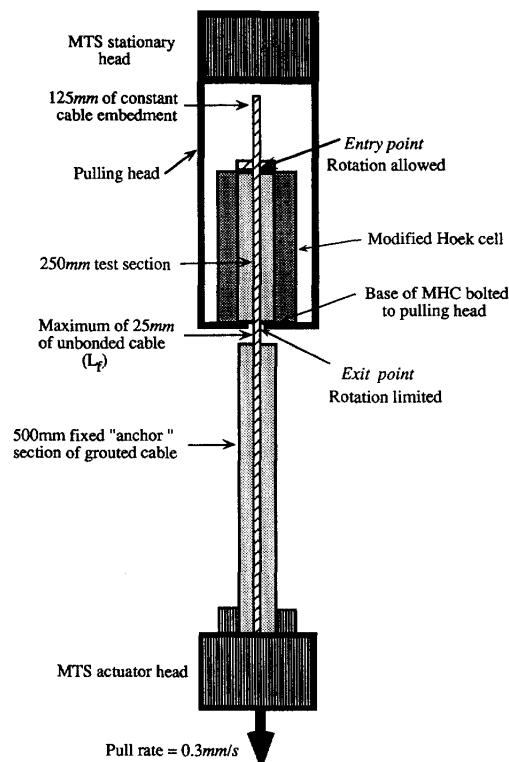| w:c ratio	σ_c (MPa)	E_g (GPa)	v_g	ϕ_g (°)	τ_0 (MPa)
0.30	79	18.6	0.2	27	18.9
0.40	58	12.1	0.2	22	15.5
0.50	45	9.3	0.2	20	11.5

Fig. 4. The pull test set-up. It is essentially identical to that used in [6].

specimen, while the latter serves only as a mould which was removed prior to testing so enabling the MHC to provide radial confinement to the outside of the grout annulus. Samples were grouted using three different w:c ratio cement pastes; 0.3, 0.4 and 0.5. The relevant physical properties of these are presented in Table 1. They fall within the previous dataset presented by Hyett et al. [14]. The samples were cured at >95% relative humidity (ASTM C511) for 28 days.

Pull test procedure

The triaxial cell was incorporated into the modified push test setup described and evaluated by Reichert [15]. This procedure is itself a derivative of the split-pipe pull test developed by Fuller and Cox [4] which has since become the accepted laboratory standard.

The complete experimental set-up is shown in Fig. 4. For each cable pull test:

—the axial displacement (u_a) was increased at a rate of 0.3 mm/sec in a stiff MTS testing frame
—the axial pullout force (F_a) applied by the testing machine was monitored
—a prescribed pressure (p_2) was maintained constant (to within 0.1 MPa) in the triaxial cell

---

†Improvements in grout pump technology have enabled many mining operations to routinely use grouts in the range 0.3–0.35 w:c for cable bolt applications.

—the radial dilation (u_{r2}) was measured by cantilever strain gauge arms within the triaxial cell.

To prevent the formation of transverse fractures, it was necessary to axially constrain the grout annulus using a specimen end cap (4 in Fig. 2) prior to the application of the confining pressure. The base of the MHC was bolted to the pulling head to prevent both eccentric loading and rotation of the sample and cell during testing. Consequently, rotation was prevented during the test at all points except the free end of the cable (Fig. 4). All deformations associated with the test frame and head attachments were subtracted so that the axial deformation is exactly that at the exit point.

The test programme (Table 2) was intended to investigate the effect of two parameters:

(i) the confining pressure applied by the MHC
(ii) the w:c cement ratio of the cement paste.

The embedment length, 250 mm, was comparable to that used by previous workers [1, 4, 8]. At the start of the test 25 mm of free cable $(L_f$ in Fig. 4) existed between the test section and the anchor section. A decision was made to conduct more tests at a 0.3 w:c ratio.† An average of four tests were conducted at each combination of parameters, and only highly circumspect results were eliminated.

EXPERIMENTAL RESULTS

Failure always occurred by slip at the cable–grout interface. A typical set of results for axial force and radial dilation (0.3 w:c, 15 MPa confining pressure) are presented in Fig. 5: the heavy line represents an average. Average results for each combination of parameters are presented in Fig. 6. Overall, the radial displacement–axial displacement data were less consistent than the axial load–axial displacement data. This was inevitable because the measurements were made at the outer surface of a fractured cement annulus, transected by radial fractures and comprising distinct wedges able to move independently of one another during a test. Nevertheless, distinct trends exist within the dataset. These are most evident for the 0.3 w:c ratio results for which more tests were performed.

Influence of confining pressure

The most obvious effect of confining pressure is to increase the bond strength, especially for confining pressures below 10 MPa. The shape of the load–displacement plots is also pressure dependent. For low confining pressures, peak capacity was attained during the initial 10 mm of axial displacement, whereas for higher confining pressures it usually occurs after 40–50 mm. The associated radial dilations decrease with confining pressure. At higher confining pressures, dilations in the range 10–20 μm, are approaching the resolution limit of the cantilever strain gauge arms.

Influence of water:cement ratio

Higher bond strengths were attained for lower w:c ratio grouts, the effect being most pronounced between

Table 2. The complete test programme

w:c ratio	1 MPa	2 MPa	3 MPa	5 MPa	10 MPa	15 MPa	Varied MPa	Total
0.30	3		5	3	3	4	2	20
0.40		2		3	4	4		13
0.50		3		4	3			10

0.3 and 0.4 w:c. However, at high confining pressures, the shape of the pull curves changed with grout w:c ratio. Results for a 0.3 w:c exhibited pronounced work hardening, whereas those for a 0.5 w:c were almost perfectly plastic. In fact, during the initial stages, the bond strength for a 0.5 w:c ratio was higher than for a 0.4 w:c which was in turn higher than for a 0.3 w:c (see Fig. 6). The effect of w:c ratio on radial dilation were also surprising. Contrary to expectation, slightly higher radial dilations occurred for weaker grouts (higher w:c ratio). It had been anticipated that higher radial

Fig. 5. Typical data obtained from a MHC cable pull test: top, pull force (F_a) vs axial displacement (u_a); bottom, radial displacement (u_{r2}) versus axial displacement (u_a). The heavy lines represents the average of the individual test results.

dilations would be generated by stronger grout flutes. Both of these apparent anomalies can be explained by the role of shrinkage during curing.

Relatively little quantitative data exist concerning shrinkage due to curing of cement paste, especially concerning the effect of w:c ratio. More is known for concretes, for which the aggregate acts to reduce shrinkage. Qualitatively, it is generally accepted that the shrinkage strain is negligible for a 0.3 w:c ratio cement paste, but increases with increasing w:c ratio. Laldji and Young [20] consider the effect of shrinkage in their model for the bond failure of concrete grouted ground anchors. They give the following relation for the compressive stress generated at the cable–grout interface due to shrinkage:

$$p_1 = \frac{E_c(r_2^2 - r_1^2)}{(r_2^2 - r_1^2)(1 - v_g) + \frac{E_c}{E_g}(r_2^2(1 + v_g) + r_1^2(1 - v_g))} \cdot \epsilon_s$$

(1)

where ϵ_s is the shrinkage strain.

For pull tests conducted in a borehole or pipe, grout shrinkage will create an initial gap between the confinement and the outer surface of the cement annulus.

INTERPRETATION OF THE EXPERIMENTAL RESULTS

Failure mechanisms

There are three conceivable mechanisms by which bond failure may occur during a pull test (Fig. 7):

(i) dilational slip accommodated by radial splitting
(ii) unscrewing
(iii) shear failure of the cement flutes.

(i) and (iii) are known to be important during the bond failure of reinforcing bars in concrete [16–19]. For cables dilational slip associated with radial splitting is known to dominate at very low p_1. During tests confined by transparent heat shrink [15], radial fractures which form after 1–2 mm of axial displacement, were observed to dilate by 2–3 mm. Figure 8 presents results from two MHC tests conducted at 1 MPa confining pressure. The distinctive elbow in the dilation profile is thought to correspond to a transition from unscrewing to dilational slip, caused by the torque that builds up during the pull test.

At slightly higher p_1 bond failure tends to occur by either unscrewing or shear failure. Figure 9 shows a series of scanning electron microscopic (SEM) micrographs from a cable pull test specimen which has undergone bond failure while confined in a Sch. 80 aluminium pipe [3]. Whereas shearing of the grout flutes is important near the exit point of the cable (i.e. the end prevented
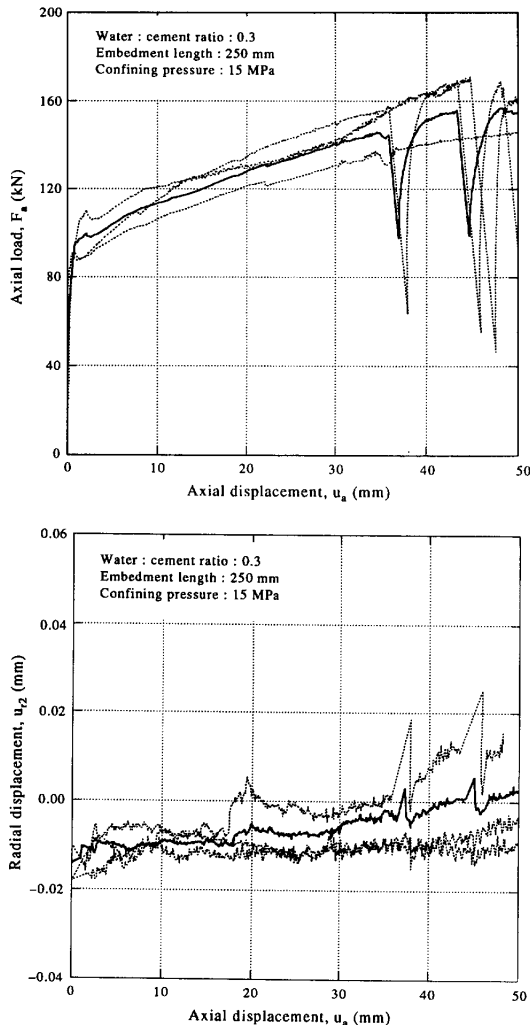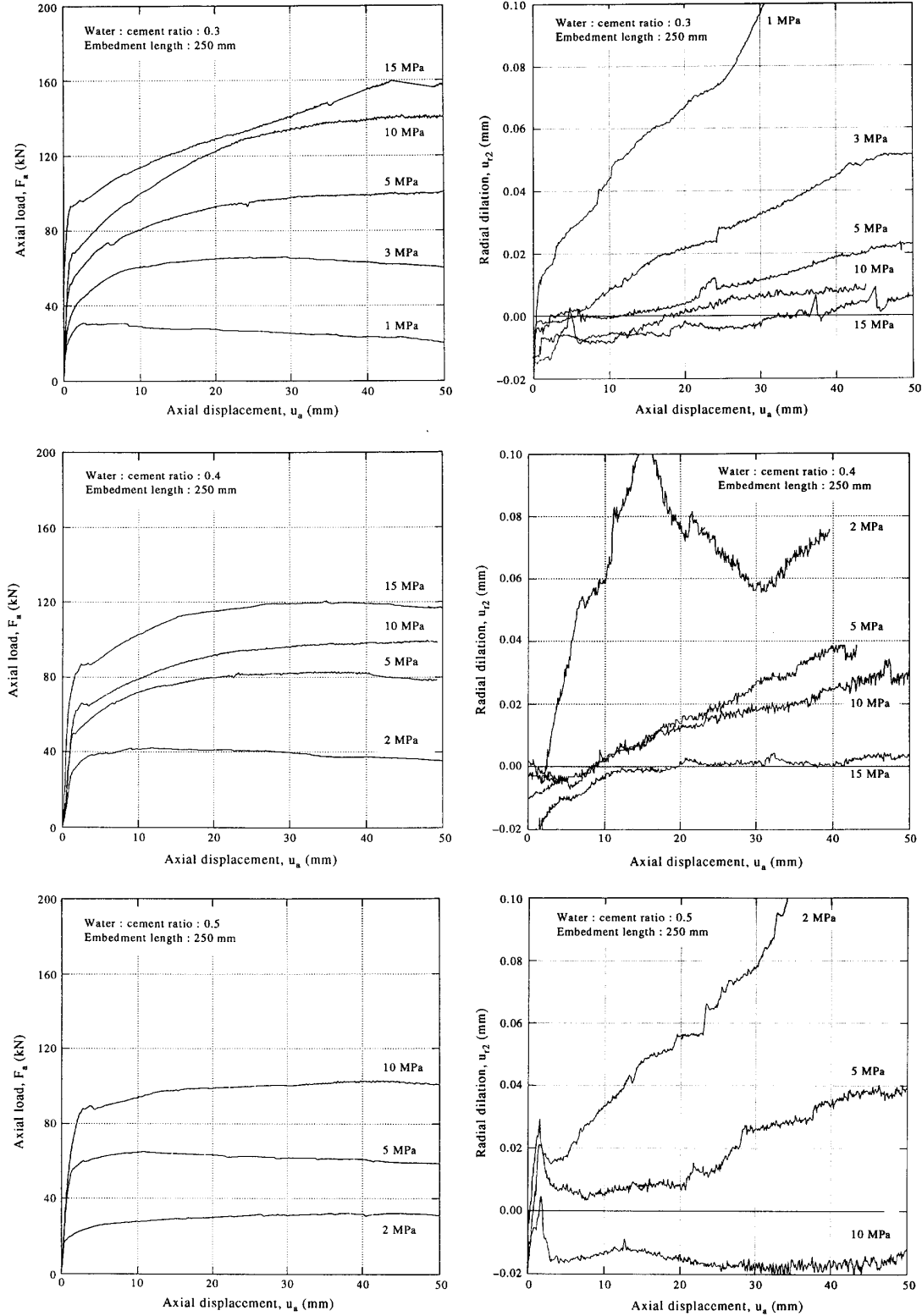
Fig. 6. Average pull test data for 0.3 (top) 0.4 (middle) and 0.5 (bottom). Axial pull force (F_a) vs axial displacement (u_a) are on the left, radial dilation (u_{r2}) vs axial displacement (u_a) on the right.

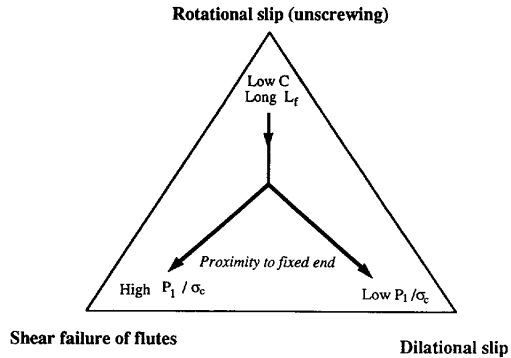Rotational slip (unscrewing)

Fig. 7. The three failure mechanisms for cable bolt bond failure C is the torsional rigity of the cable, L_f is the free length between the test section and anchor point and σ_c is the UCS of the grout.

from rotating), 75 mm away the grout flutes are almost completely undamaged. Thus, along the majority of the test section bond failure occurs by unscrewing rather than shear failure of the grout flutes: quite different from a solid bolt or bar. Tests conducted in an Instron rotational testing frame [3], revealed that the torsional rigidity of 15.2 mm (0.6″) seven-wire strand was approx. 16,000,000 N mm², or 1–2 orders of magnitude less than the corresponding value for a solid bar of the same nominal diameter manufactured in the same material. This, combined with the pronounced helical geometry of the outer wires, is responsible for the different failure mechanisms for grouted cables.

As further evidence of the importance of unscrewing, immediately following a cable pull test conducted in either the laboratory or the field, a sometimes violent rotation of the specimen occurs as the load is released. From geometric considerations the amount of rotation should be:

$$\theta = \frac{2\pi u_a}{l} \qquad (2)$$

where l is the pitch length of the cable.† So for 50 mm of axial displacement a 70° rotation should accompany unloading. Although, the actual measured values are usually 10–20° lower than this value, rotations in excess of 50° do demonstrate the importance of unscrewing during bond failure.

In practise, all three of the failure mechanisms outlined above occur concurrently. Thus, even at the highest confining pressures when the role of dilation is most constrained, the radial fractures that accommodate dilational slip are always present.

Progressive cable bolt bond failure

The load–displacement plots presented in Fig. 6 do basically confirm that the failure process can be divided into four distinct stages. However, in previous

---

†219 mm for the cable used in this research, though it may vary from 192 to 232 mm for different manufacturers. ASTM A416 for uncoated seven-wire stress relieved steel strand for prestressed concrete stipulates 189–253 mm or 12–16 times the nominal diameter.

descriptions of progressive bond failure [6], the important role played by unscrewing was not fully appreciated.

Stage 1 ($u_a < 1\,mm$). The essentially linear response that characterizes the initial stage of a cable pull test is related to the axial stiffness of the cable, the elastic properties of the grout and the properties of the interface between the two. Figure 10 indicates that the initial stiffness is sensitive to the confining pressure, as is the onset of non-linearity in the load–displacement plot. Both of these observations confirm that the bond, even during this initial stage, is related to frictional–mechanical rather than adhesional resistance.

Stage 2 ($u_a < 1\,mm$). Near the fixed end of the test section, where the bond will begin to break first and unscrewing is restricted, only limited slip can occur at the grout–cable interface unless either (i) radial fracturing of the grout annulus splits it into distinct wedges, which can then be radially displaced to allow dilational slip, or (ii) shear failure through the cement flutes occurs.

The initiation and stable propagation of one or both of these mechanisms is responsible for the reduction of axial stiffness and defines the onset and the extent of stage 2.

Stage 2–stage 3 transition (splitting of the cement annulus, $u_a = 1\,mm$). A pronounced change in stiffness, often accompanied by a drop in capacity, and an audible emission from the specimen, occurs after 1–2 mm of axial displacement. It is proposed that this corresponds to splitting of the cement annulus. In some tests this appears to have occurred instantaneously; in others the fracturing was more progressive, either because individual fractures were propagating intermittently, or more likely because different fractures become unstable at slightly different axial displacements.

The splitting process was more unstable for higher w : c ratio grouts, and, because these are known to shrink more during curing, the associated tensile tangential stress may contribute to that required to split the cement annulus. In some cases for a 0.5 w : c ratio, incipient radial fractures were observed in the sample prior to testing. After the cement annulus is fully split, the stored elastic strain energy in the annulus due to shrinkage must be released, and the individual grout wedges will have a tendency to extend in the radial direction and contract in the tangential direction, prematurely opening the radial fractures. This effect can explain the high bond strengths for higher w : c ratio grouts during the early stages of the pull test ($u_a < 10\,mm$ in Fig. 6).

Figure 11 shows details for three individual tests conducted at different confining pressures. Notice the jump in radial dilation associated with radial splitting, and whereas, at high confining pressures this is almost completely recovered, at low confining pressure it is not.

Stage 3 ($u_a = 1$–$50\,mm$). Research has established that stage 3 is the most critical part of the cable bolt bond failure process, and that the associated failure mechanism is highly sensitive to the radial confinement. For the MHC tests, the frictional resistance to pullout must be controlled by:
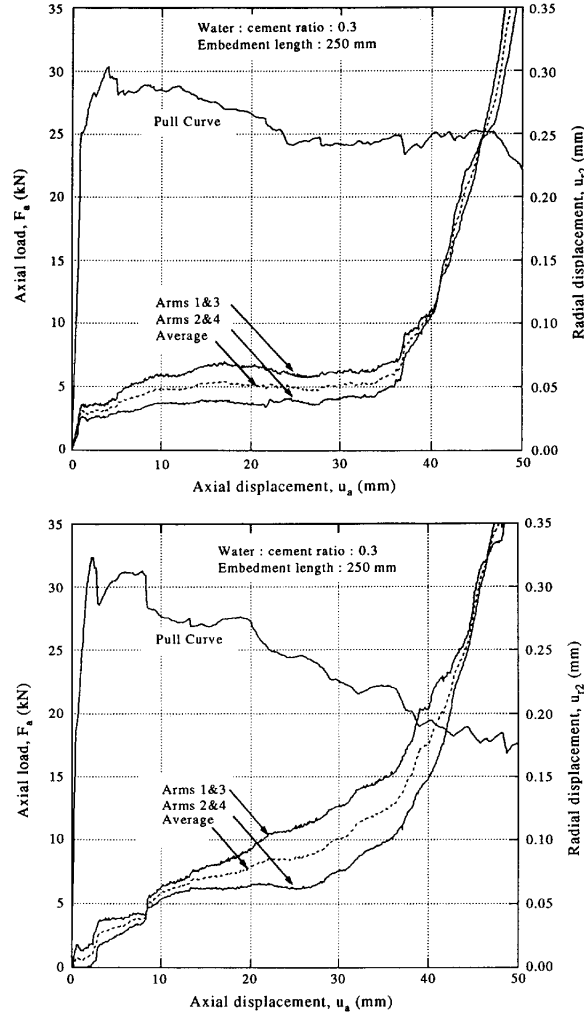
Fig. 8. Results for specimens HP031-1 and HP033-1, for a 0.3 w:c ratio grout with a confining pressure of 1 MPa. A pronounced elbow is observed in the dilation data at around 35 mm of axial pull. This is thought to correspond with a transition from rotational to dilational slip.

(i) the frictional properties at the cable–grout interface; and,

(ii) how much stress is transferred through the grout annulus, from the outer surface where the confining pressure is maintained constant to the cable–grout interface where cable slip is actually occurring.

As will be outlined in the mathematical model presented below, the work hardening exhibited during stage 3 of the load–displacement plots can be explained by an increase in the radial stress transferred through the cement annulus as the wedges that comprise it are progressively forced apart, due to dilation at the cable–grout interface.

For unscrewing failure during stage 3, the torque generated in the length of cable between the test and anchor sections progressively increases according to:

$$T = \frac{C\theta}{(u_a + L_f)} = \frac{2\pi C u_a}{l(u_a + L_f)} \tag{3}$$

where C is the torsional rigidity of the cable, l is the pitch length of the cable and L_f is the initial free length (the length exists between the test section and where the cable is gripped at the start of the test—in these tests 25.4 mm). Note that for tests in which a significant free length exists, or for a loosely wound cable with low C, less torque will develop for a given u_a and the cable will be able to unscrew even at the exit point. Hence, less shearing of the grout flutes and less dilation will result in less work hardening during stage 3 (i.e. a nearly perfect plastic response, e.g. see the test results in [8] and [10]) and consequently, lower bond strengths: similarly, for loosely wound cables with a low C.

Stage 4 ($u_a > 50\,mm$). The ultimate capacity and maximum radial dilation are usually attained after 40 or

50 mm of axial displacement. Thereafter, the dilation recorded by the strain gauge arms does not continue to increase.

MODELS FOR CABLE BOLT FAILURE

Instinctively, it may seem that the regular geometry of a fully-grouted cable bolt should facilitate a mathematical approach. Indeed, Burns [21] presents an elastic treatment of the splice joints within cable-reinforced conveyor belts. He states that "a cable when pulled,

has a tendency to twist", and proceeds to consider the interaction between axial load and torque along the embedded cable when it is pulled from an incompressible elastic half space. Based on an analysis of the forces generated as a fully-bonded cable is pulled, Tan [22] also predicts the tendency for the cable to twist when pulled.

If progressive bond failure at the grout–cable interface is also considered, the problem becomes significantly more involved. In certain ways it becomes similar to the frictional shear failure of any irregular interface. Thus,
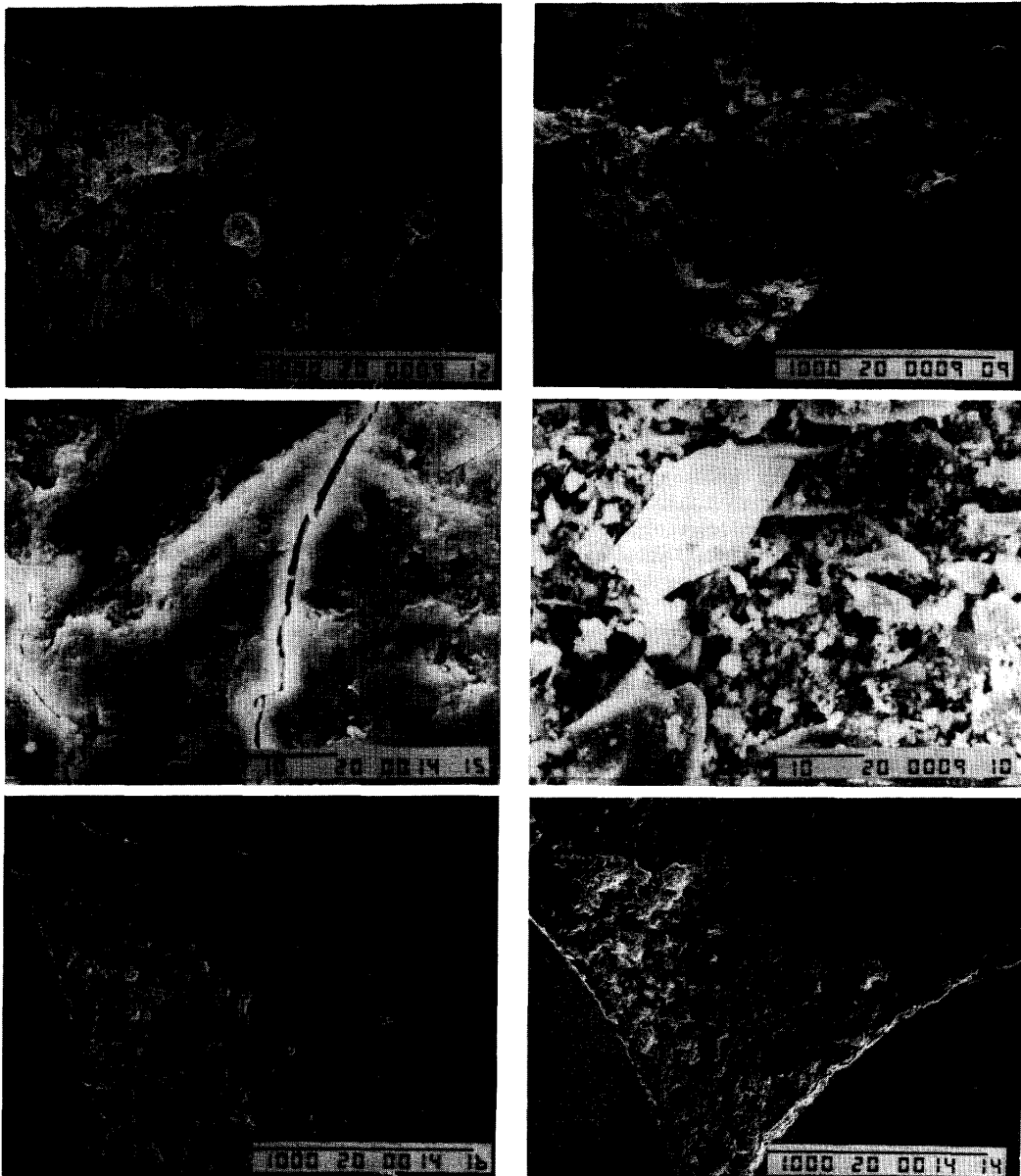

Fig. 9. Scanning electron micrographs for a specimen that has undergone bond failure in an aluminium pipe. Top, section 25 mm from the exit point of the test section; middle, detailed micrograph of the degradation and fracturing; bottom, same flutes but at 75 mm from exit point.
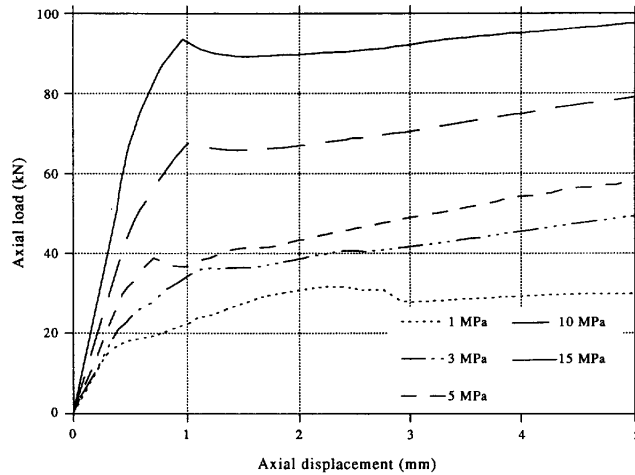
Fig. 10. Axial pull force (F_a) vs axial displacement (u_a) for the first 5 mm of pullout -0.3 w:c ratio.

the contributions of Newland and Allely [23] for granular media, and Jaeger [24], Ladanyi and Archambault [25] and Goodman [26] for rock joints provide guidance and insight.

As stated by Saeb and Amadei [27], the mechanical response of any rough interface to shear loading depends most critically on the surface morphology, the strength of the irregularities/asperities and the boundary conditions applied normal to the surface. Goodman [26] predicted that a joint shear test conducted under restricted normal displacement conditions would result in a higher shear strength than one conducted under conditions of constant normal stress. Laboratory tests by Leichnitz [28] and Archambault et al. [29] have since confirmed this. Important recent developments [27] in the rock joint literature have demonstrated that an adequate representation of joint response under any boundary conditions can be derived from tests conducted under constant normal stress.

Although such comparisons are valuable, it is important not to oversimplify or distort the problem, in order to force agreement between the mechanics of cable bolt bond failure and apparently analogous problems. Cable bolt bond failure is quite distinct from shear failure of a rock joint, or even bond failure of deformed bars. In fact, it is within these fundamental differences that many of the answers to inadequate cable bolt performance are to be found.

GRAPHICAL MODEL

Using the experimental results presented above, and essentially following the approach taken for rock joints by Goodman and Boyle [30] and Saeb and Amadei [27] for rock joints, a series of response curves can be constructed. Similar representations have been used by Leichnitz [28] for rock joints and by Yazici and Kaiser [31] for cable bolts.

In Fig. 12, the MHC test data for a 0.3 w:c ratio, when plotted in quadrants 1 and 3 (Q1, Q3) has been

used to construct the appropriate response curves in quadrants 2 and 4 (Q2, Q4). Notice that the axial load has been retained rather than dividing by the apparent contact area to obtain an axial shear stress. The completed construction is shown in Fig. 13.

In quadrant 2:

(i) envelopes are shown for a 10 mm increment of axial pull. The uppermost envelope represents the change in peak capacity with confining pressure. The curves for different axial displacements lie over one another for low confining pressures indicating an almost perfect plastic response, whereas at higher confining pressures divergence of the curves is indicative of work hardening behaviour;

(ii) though linear below 5 MPa, the effect of confining pressure on peak capacity decreases at higher radial confining pressures. As discussed below, if the pull force (F_a) is divided by the apparent contact area at the grout–cable interface, the linear segment provides an estimate of the average friction angle (ϕ') at the interface along the test section.

In quadrant 4:

(iii) the line AB represents the radial deformation of the intact annulus as the radial confining pressure is applied (i.e. its slope is the radial stiffness of the intact annulus);

(iv) the slope of the other curves, $u_a = 10, 20, 30, 40$ and 50 mm, represents the radial stiffness of the cable–bolt system (grout annulus, cable–grout interface and cable) as the cable is progressively pulled. The radial stiffness decreases with axial displacement especially at low confining pressures. For $u_a = 10$ mm the radial stiffness of the grout annulus is almost constant below 3 MPa and above 10 MPa: the former approximately corresponds to the radial stiffness of the
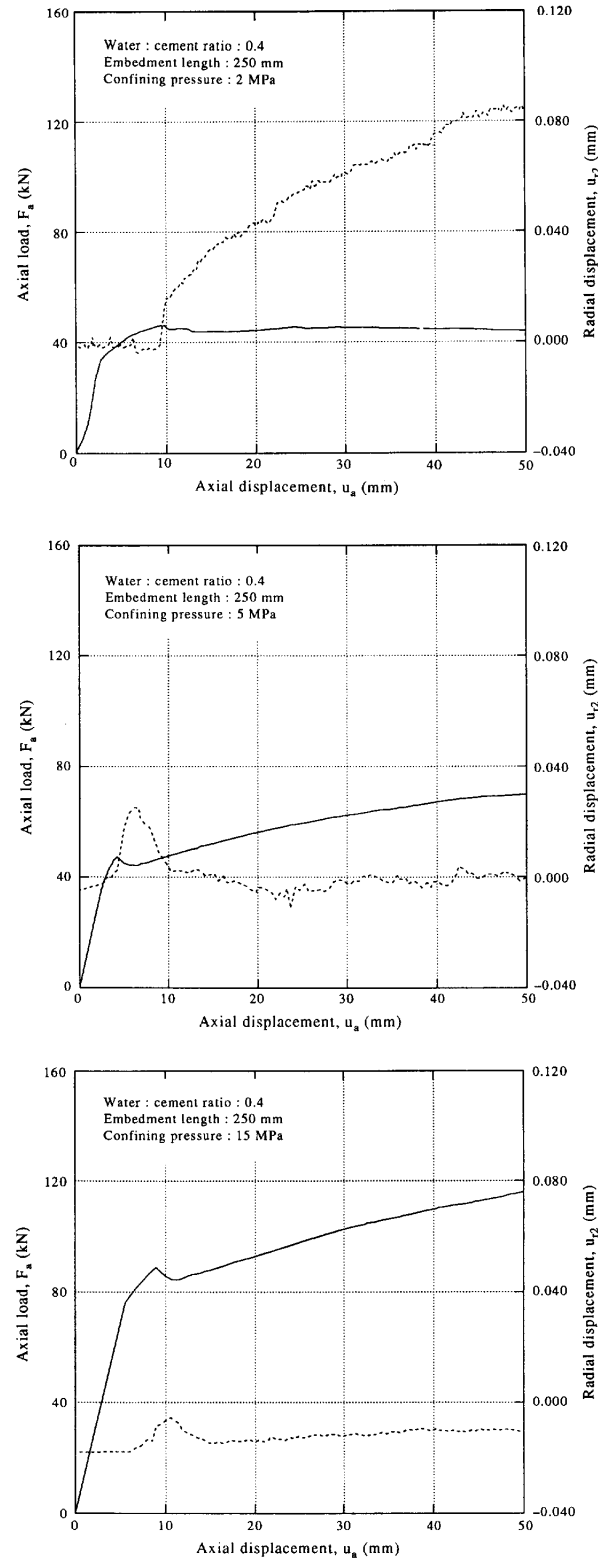
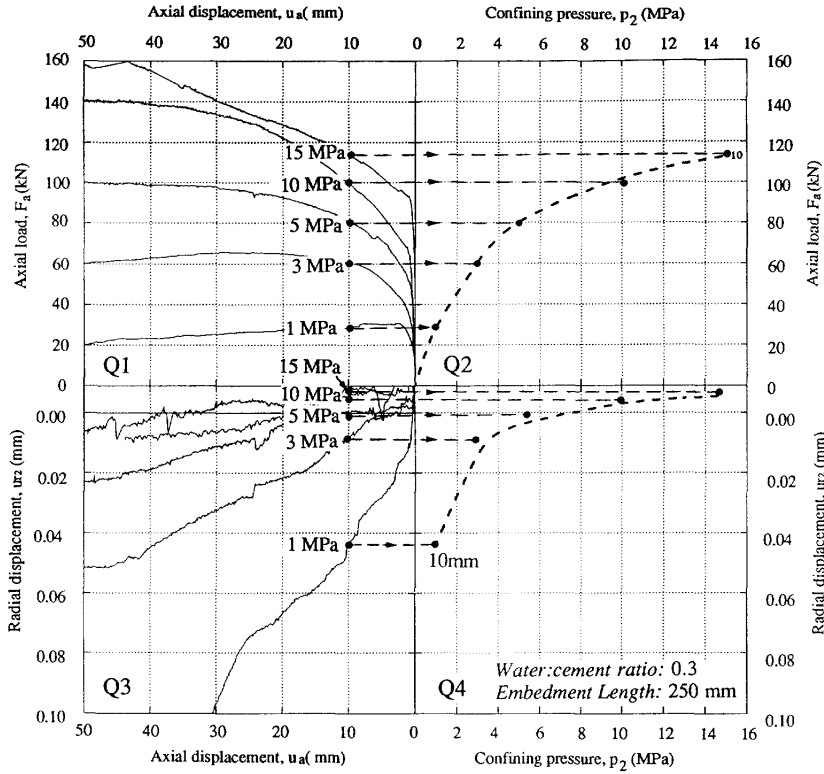Fig. 11. Pull test results at different confining pressures.

Fig. 12. Construction of response curves for $u_a = 10$ mm using the MHC pull test results.

independent grout wedges bearing against the cable–grout interface (i.e. the confining pressure is insufficient to close the radial fractures) and the latter to the radial stiffness of the intact annulus (i.e. the confining pressure is high enough to close radial fractures). In between, the stiffness progressively increases as the radial fractures are closed by the confining pressure.

The ability of the model to simulate bond strength for radial stress paths associated with more realistic radial boundary conditions likely to occur at the borehole wall in operational practice will be evaluated below.

Cable bolt bond failure under constant radial stiffness

Hyett et al. [6] presented results from a series of cable pull tests conducted under the condition of constant radial stiffness in 2″ Sch. 80 steel, aluminium and PVC pipes (Fig. 14). For these, higher cable capacities were observed for tests conducted in pipes of higher radial stiffness. The graphical construction for the aluminium tests is shown in Fig. 15, and results for all three confinements are presented in Fig. 16. A comparison between Figs 14 and 16, indicates a good agreement.

Cable bolt bond failure under variable radial pressure

Several MHC cable pull tests were conducted in which the radial confining pressure was varied during a single test. For HP034-5 the pressure was increased from 1 MPa at the beginning of the test to 3, 5 and 10 MPa over 50 mm of axial displacement. For HP033-5 the pressure was successively reduced from 10 MPa at the beginning of the test to 5, 3 and finally 1 MPa. The axial load (F_a) and radial displacement (u_{r2}) responses are indicated in Fig. 17. For both tests the model is able to realistically simulate the cable bolt bond failure response (Fig. 18), and especially the variations in radial displacement. For HP034-5, it overestimated the load at higher confining pressures, especially 10 MPa $(u_a > 40$ mm), which may reflect its inability to properly represent the accumulation of damage to the grout flutes under different load paths. Further testing is required to confirm this.

MATHEMATICAL MODEL

The graphical model and the constructions associated with using it provide insight into the frictional–dilational mechanics of cable bolt bond failure. In the next section, an equivalent mathematical model will be introduced. The theory presented provides generality through the inclusion of appropriate operational and physical parameters (i.e. hole size, grout properties, cable characteristics etc). The sign convention used is shown in Fig. 19. The formulations presented are suitable for implementation into numerical models, so providing the potential to realistically simulate the
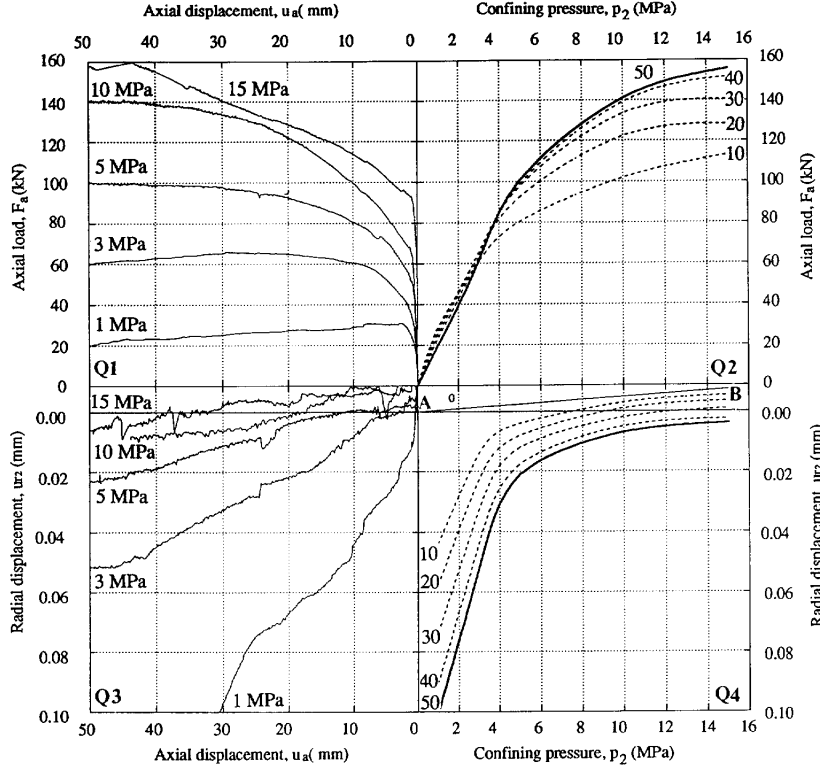
Fig. 13. Complete cable bolt bond failure response curves for a 0.3 w:c ratio, opposite the MHC data from which they were determined. Similar curves can be determined for a 0.4 and 0.5. Further details are explained in the text.

complex interaction between the rock mass surrounding an excavation, not just for a single cable, but for an array or pattern of cables designed to reinforce it.

The Cable–Grout Interface

Splitting of the cement annulus

As explained under the same subheading above, splitting of the grout annulus which occurs after approx. 1 mm of axial pull, has the potential to generate dilations in the order of 10–20 μm. However, if a high radial confining pressure is applied to the outside of the cement annulus, an almost instantaneous reversal occurs. Hence, at high confining pressures radial splitting may result in no radial dilation. If the pressure-dependent closure is assumed to be hyperbolic (as for the normal closure of a mated rock joint) then the total dilation due to splitting may be written as:

$$v_{sp} = v_0 - \frac{p_1 \cdot v_0}{(K_0 \cdot v_0 + p_1)} \qquad (4)$$

where v_0 is the dilation generated by splitting when $p_1 = 0$, and K_0 represents the radial stiffness (MPa/mm) of the cable–grout interface immediately following splitting, when $p_1 = 0$ also. Appropriate values for K_0 and v_0 can be determined from the radial displacement–axial displacement plots in Fig. 6. Using the 0.3 w:c ratio results which are better constrained, at 1 MPa approx.

10 μm of radial displacement occurs due to splitting, for 3 MPa, 3 μm and for higher confining pressures a negligible amount. Based on these limited data, v_0 was determined to be 35 μm and K_0, 30 MPa/mm. Since the cable is not rigid, v_{sp} is related to the radial displacement at the inner surface of the grout annulus (u_{r1}) by:

$$u_{r1} = v_0 - \frac{p_1 \cdot v_0}{(K_0 \cdot v_0 + p_1)} - \frac{p_1}{K_{rc}} - \frac{F_a v_c}{2\pi r_1 E_c} \qquad (5)$$

where the third and fourth terms describe the radial contraction of the cable directly related to the application of p_1, and the radial contraction caused by the Poisson effect as the cable is pulled axially. In the former, K_{rc} represents the radial stiffness of the cable itself perpendicular to its axis. Assuming this section is solid, and not composed of seven individual wires with limited contact areas, will result in an over-estimation of K_{rc}. Furthermore, cables from certain manufacturers appear to be wrapped more tightly than those from others. In the absence of reliable data, a value for K_{rc} of 2500 MPa/mm was indirectly determined based on a best fit with the MHC results. This is approximately an order of magnitude less than if a value has been determined based on the axial value of E_c (140 GPa) for an equivalent bar of the same nominal diameter. The fourth term in equation (5), describes the radial contraction at the midpoint of the specimen (i.e. where the cantilever
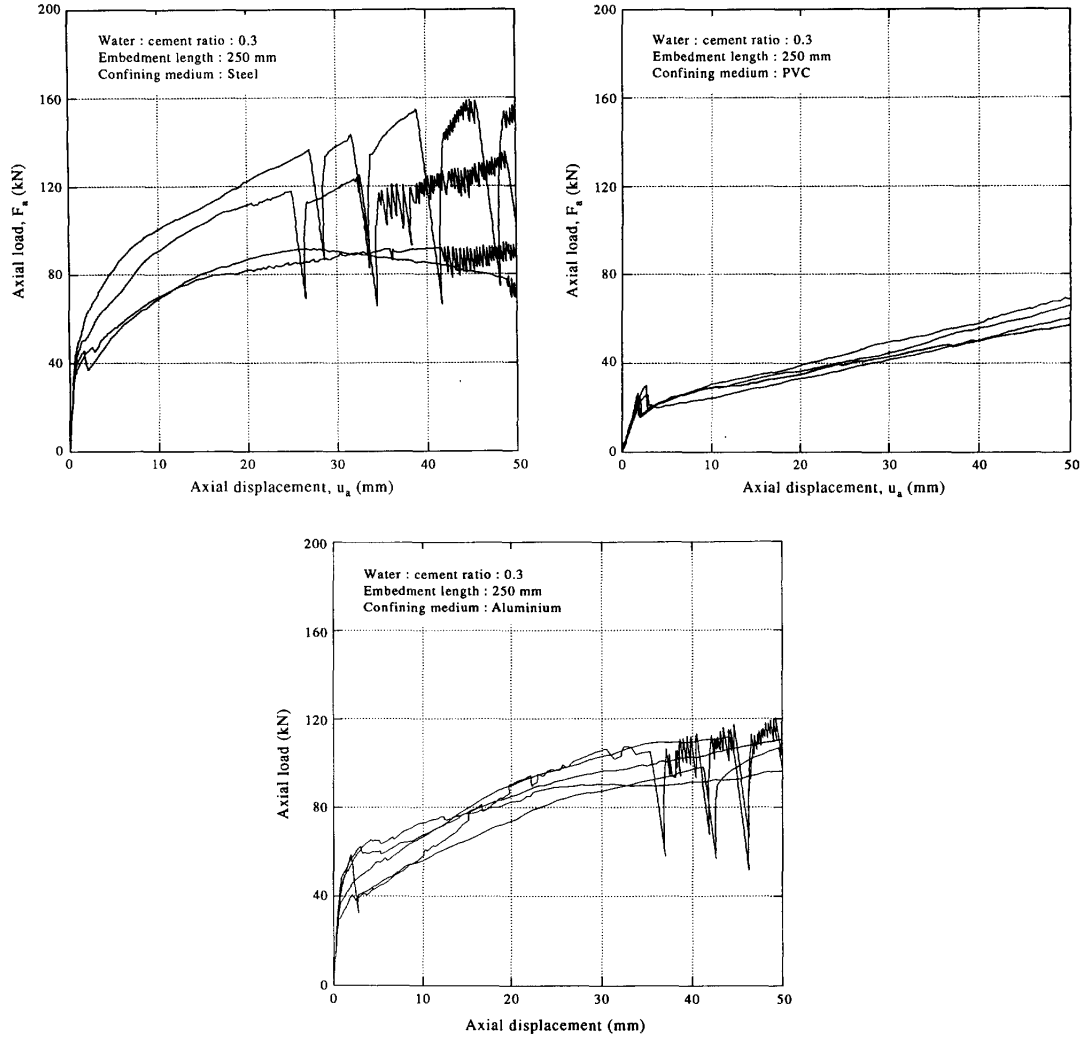
Fig. 14. Laboratory cable pull test results for a 0.3 w:c ratio grout confined using Sch. 80 steel, PVC pipes and aluminium.

strain gauge arms were located), assuming a linear decrease of the pull out force along the test section immediately after splitting. However, Stillborg [8] performed tests on seven-wire strand cable, and determined its Poisson's ratio to be low ($v_c = 0.02$); therefore:

$$u_{r1} = v_0 - \frac{p_1 \cdot v_0}{(K_0 \cdot v_0 + p_1)} - \frac{p_1}{K_{rc}} \tag{6}$$

provides an acceptable approximation.

Friction coefficients

The axial force corresponding to the three failure mechanisms described in the interpretation of results presented above are:

for dilational slip, after splitting of the cement annulus;

$$F_a = A_1 p_1 \tan(\phi_{gs} + i) \tag{7}$$

for non-dilational unscrewing;

$$F_a = \frac{A_1 p_1 \tan \phi_{gs}}{\sin \alpha} + Q \tag{8}$$

and, for shear failure of the cement flutes:

$$F_a = A_1 (\tau_0 + p_1 \tan \phi_g). \tag{9}$$

In which ϕ_{gs} is the sliding friction between grout and steel, ϕ_g is the internal angle of friction for grout and τ_0 is the grout cohesion. Q is the component of the pull out force required to untwist the free length of cable, which, based on work considerations, is given by:

$$Q = \frac{4\pi^2 C u_a}{l^2(u_a + L_f)} \tag{10}$$

Now, it has been proposed, that, with the exception of tests conducted at 1 MPa ($u_a > 30$ mm), bond failure occurs predominantly by unscrewing, except over a
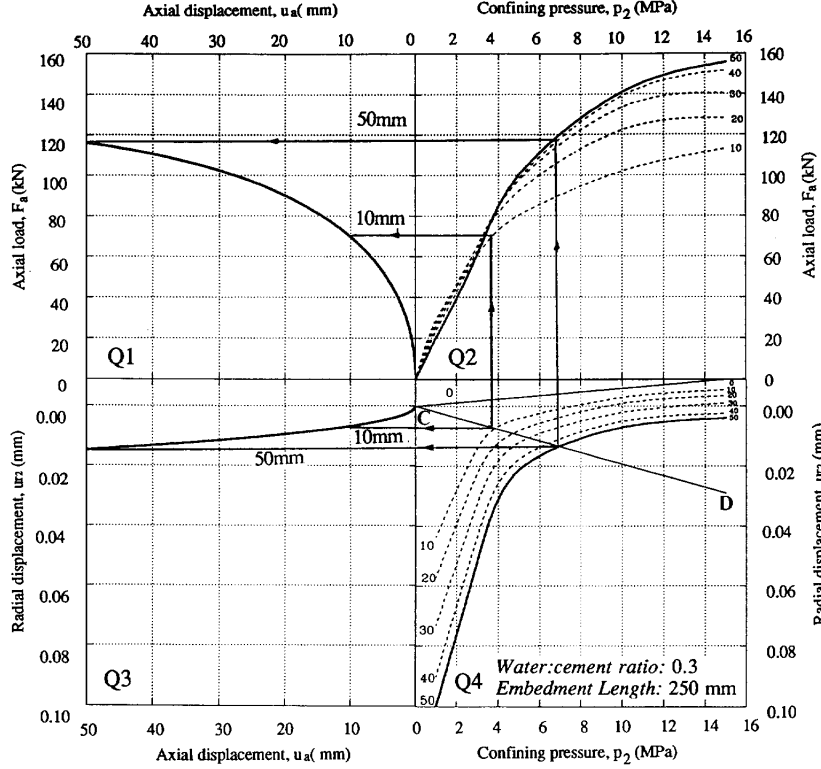
Fig. 15. Construction of the bond failure response for a pull test at 0.3 w:c ratio confined in a Sch. 80 aluminium pipe. The straight line (C–D) in quadrant 4 corresponds to the radial stiffness at the inside of the pipe.

restricted length near the fixed end where shear failure of the cement flutes is important. Since the dilation angles are so small ($i < 0.2°$), the pull force component related to dilational slip may be ignored, and using an approach similar to [25], the axial pull out force may be approximately written as:
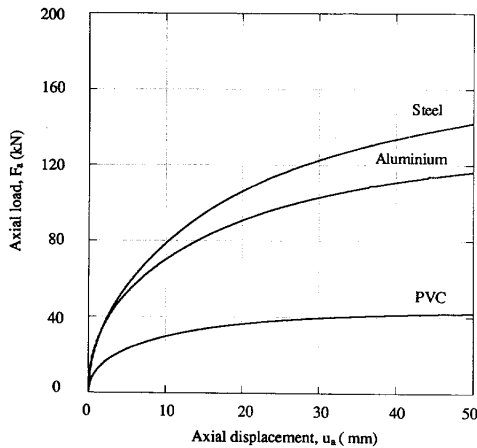

Fig. 16. Predicted cable bolt bond failure response for Sch. 80 steel, aluminium and PVC pipes. These can be compared with the corresponding pull test results in Fig. 14.

$$F_a = \frac{L_s}{L_c} \cdot A_1(\tau_0 + p_1 \tan \phi_g) + \left(1 - \frac{L_s}{L_c}\right)$$
$$\times \frac{A_1 p_1 \tan \phi_{gs}}{\sin \alpha} + Q(L_s < L_e) \quad (11)$$

where L_s is the length over which shear failure occurs. The parentheses following Q imply that this term should be added for cases in which any length of the test section, however short, fails by unscrewing.

Presently, no rational basis, either theoretical or experimental, exists for the determination of L_s. Presumably it must depend on an interplay between the torque generated in the free section during bond failure and the strength of the cement flutes. To avoid the problem, the concept of an average coefficient of friction (ϕ') over the whole test section is usually introduced [31, 32]. Assuming that untwisting is important, and knowing that i is very small ($<0.2°$), then,

$$F_a = A_1 p_1 \tan \phi' + Q \quad (12)$$

Figure 20(a) plots $(F_a - Q)/A_1$ against p_1 [determined using equation (45) below which is only strictly applicable to the initial linear portion of each curve for which the radial fractures in the grout annulus are open] for different w:c ratios. The slope of the linear portion provides an estimation of ϕ' for 0.3(23°), 0.4(17°) and 0.5(15°) w:c ratios. It is assumed to be
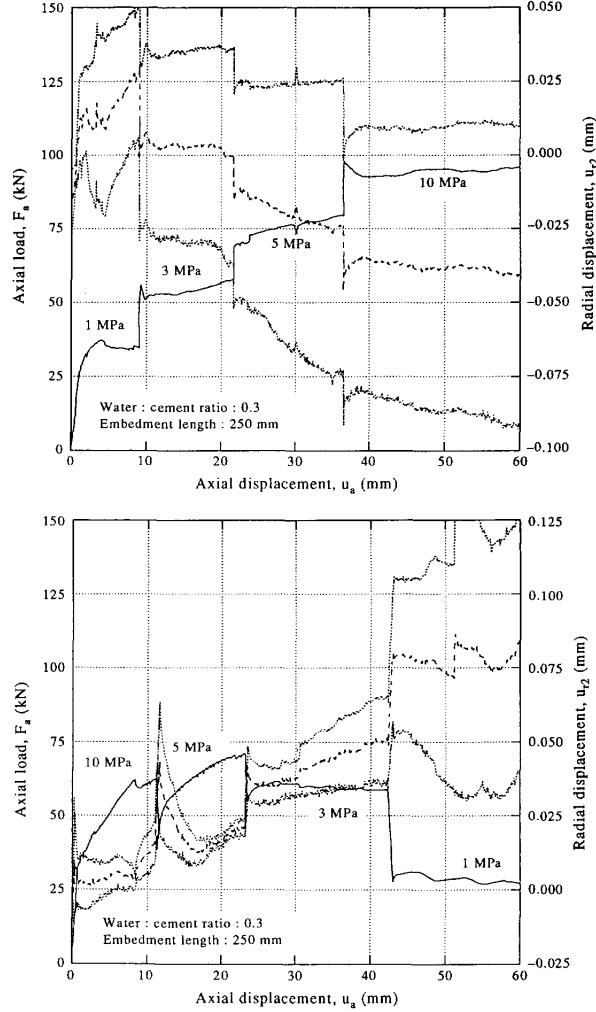
Fig. 17. Pull test results for test conducted under variable radial confining pressures: (top) HP034-5; 1–3–5–10 MPa over 50 mm of axial pull and (bottom) HP033-5; 10–5–3–1 MPa over 50 mm of axial displacement.

independent of confining pressure. Thus, the experimentally determined values for ϕ' are significantly higher than the coefficient of sliding friction for smooth steel cement surfaces in contact ($\phi_{gs} = 10$–$12°$) [20, 32]. If (11) is equated with (12), for a specified embedment length, and given grout properties, the corresponding values of L_s can be back-analysed, as a function of p_1 and grout w:c ratio. Doing this, L_s is found to increase with confining pressure and to be 25–35 mm at high confining pressures [see Fig. 20(b)], which is comparable with the extent of shearing indicated by the SEM micrographs (Fig. 9).

To reiterate, the average friction angle determined from pull tests with 250 mm embedment length varies from 23° for a 0.3 w:c ratio grout to 15° for a 0.5, and is significantly higher than that for sliding between grout and steel (10–12°). The difference can be explained by shear failure of the cement flutes in the vicinity of the exit point.

Dilation angles

Several workers have suggested that it should be possible to relate the radial deformation induced during bond failure to the geometry of the cable. Yazici and Kaiser [31] used a relation of the form:

$$v = \left(1 - \frac{p_1}{\sigma_c}\right)^k h_0 \tag{13}$$

where h_0 is given by the "height of the grout teeth", which should be approximately equal to the radius of the outer wires (2.65 mm for a 15.8 mm seven-wire strand), although in [31] a value of 0.2 mm was found to provide a better fit to experimental results. Equation (13) implies that bond failure is occurring by two mechanisms: (i) dilation-slip and (ii) shearing of the cement flutes. k is given by B/σ_c. A best fit value for B, back-analysed from test results under constant radial stiffness, was found to be 628, resulting in k values of 8–15 depending on the compressive strength of the grout. In related research,
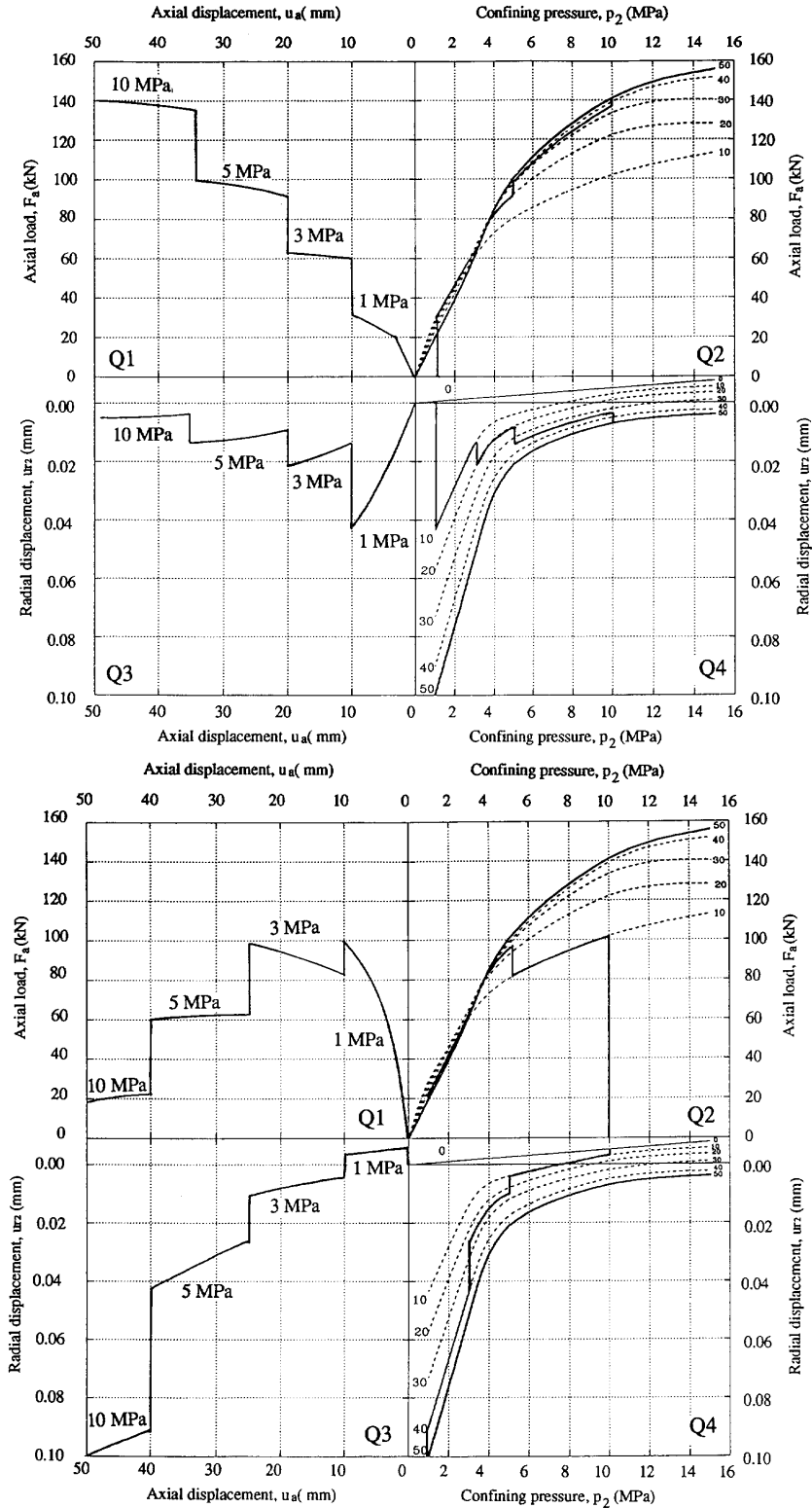
Fig. 18. Predicted cable bolt bond strength response for variable radial confining pressure tests: (top) HP034-5 and (bottom) HP033-5.
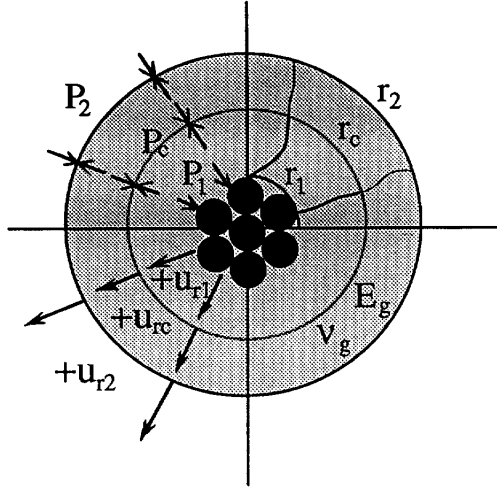
Fig. 19. Terminology and sign convention used in the mathematical model. Compressive stresses are positive, and outward directed displacements are positive. As throughout this paper, the subscript 1 applies to the inner surface of the cement annulus and the subscript 2 to the outer surface. The subscript c is explained in the text.

Ladanyi and Archambault [25] used a much lower value of k for rock joints ($k = 4$), while Chiu and Dight [33] found an even lower value ($k = 3$) applicable to rock socketed piles. Based on the discussion above, it is proposed that this inconsistency arises because equation (13), and the subsequent bond strength model (BSM) developed in [31], fails to account for the involvement of unscrewing during bond failure; this mechanism, and not shear failure of the cement flutes, is responsible for the very low dilation angles required to explain previous experimental results. Recently, an attempt has been made to incorporate the effect of rotation into the BSM [34], by invoking lower dilations (i.e. lower k) if rotation is allowed.

From Fig. 6, three important characteristics of the radial displacements that were measured at the mid-point of the test section are:

(i) an approximately linear increase with u_a;
(ii) a decrease with p_1
(iii) no significant change with grout quality.

Although the latter was not predicted, in retrospect, the grout strength should only effect that portion of the cable for which shear failure of the grout flutes occurred, namely, the 25–50 mm closest to the fixed end. Since the dilations were measured at the midpoint of the test section, (iii) can be explained.

It is our experience, that the mechanisms responsible for the dilation, and in particular the interplay between dilation and unscrewing when the latter is dominant, are so inadequately understood, and the input parameters to such an analysis so poorly constrained, that the best approach is to use the experimental data presented above, to determine an empirical relation for radial

displacement during bond failure. Based on observations (i)–(iii) assume very simply:

$$u_{r1} = \frac{k_1}{p_1} \cdot (u_a - 1) + f(p_1) \tag{14}$$

where k_1 is an empirical constant, determined by a best fit to the experimental dilation data to be 0.012 MPa. When $u_a = 1$ mm (i.e. immediately following splitting) the total radial dilation must be given by equation (6), and hence $f(p_1)$ is simply the radial displacement due to splitting. Therefore:

$$u_{r1} = \frac{k_1}{p_1} \cdot (u_a - 1) + v_0 - \frac{p_1 \cdot v_0}{(K_0 \cdot v_0 + p_1)} - \frac{p_1}{K_{rc}} \tag{15}$$

which is assumed to represent an average along the whole embedment length.

As realized by Saeb and Amadei [27], an equation of the form of (15) can be written as:

$$p_1 = \frac{(u_{r1} - w) \cdot K_0 \cdot v_0}{v_0 + (u_{r1} - w)} \tag{16}$$

(a)

(b)
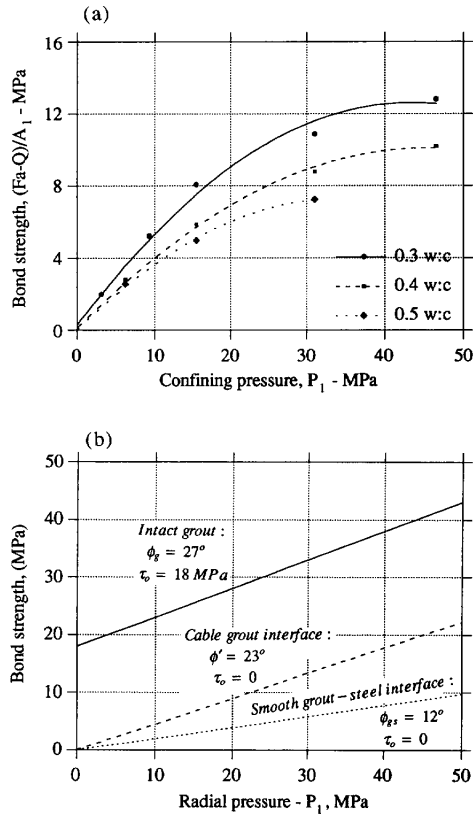
Fig. 20. (a) Average bond strength $(F_a - Q)/A_1$ vs pressure at the cable–grout interface (p_1) determined using equation (45). The initial linear portion of the plot gives the average friction angle (ϕ') for the cable grout interface. (b) The internal friction angle for the intact grout, friction angles for the cable grout interface and sliding of smooth steel and cement in contact. As explained in the text, the friction angle for the cable–grout interface (ϕ') is intermediate between the other two.

where, in the present analysis, w, which comprises both the dilation due to shearing and that related to the deformability of the cable in the radial direction, is given by:

$$w = v_0 + \frac{k_1}{p_1}(u_a - 1) - \frac{p_1}{K_{rc}} \qquad (17)$$

Equation (15) models the radial deformability of the cable–grout interface after the cable has been pulled by an amount u_a. Its form is shown in Fig. 21.

Deformability matrix for the cable–grout interface during bond failure

As u_{r1} depends on both p_1 and u_a, an incremental formulation can be obtained by differentiating equation (15)

$$du_{r1} = \frac{k_1}{p_1} \cdot du_a - \left(\frac{k_1}{p_1^2} \cdot (u_a - 1) \right.$$
$$\left. + \frac{K_0 v_0^2}{(K_0 \cdot v_0 + p_1)^2} + \frac{1}{K_{rc}}\right) \cdot dp_1 \qquad (18)$$

or after rearrangement

$$dp_1 = \frac{\dfrac{k_1}{p_1} du_a - du_{r1}}{\left(\dfrac{k_1}{p_1^2} \cdot (u_a - 1) + \dfrac{K_0 v_0^2}{(K_0 \cdot v_0 + p_1)^2} + \dfrac{1}{K_{rc}}\right)} \qquad (19)$$

Since:

$$dp_1 = \frac{\partial p_1}{\partial u_a}\bigg|_{u_{r1}} \cdot du_a + \frac{\partial p_1}{\partial u_{r1}}\bigg|_{u_a} \cdot du_{r1} \qquad (20)$$

then:

$$\frac{\partial p_1}{\partial u_{r1}}\bigg|_{u_a} = \frac{-1}{\left(\dfrac{k_1}{p_1^2} \cdot (u_a - 1) + \dfrac{K_0 v_0^2}{(K_0 \cdot v_0 + p_1)^2} + \dfrac{1}{K_{rc}}\right)} \qquad (21)$$
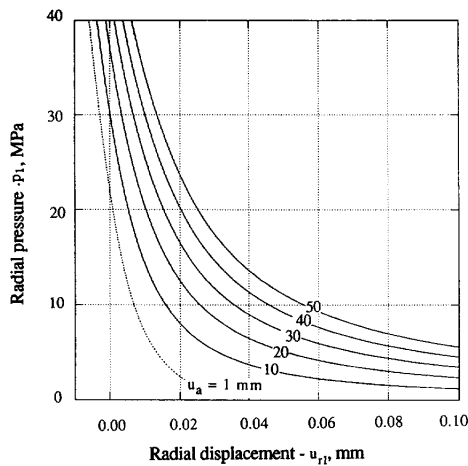

Fig. 21. The form of equation (15) (p_1 vs u_{r1} space). A similarity with quadrant 4 (p_2 vs u_{r2}) of the graphical method is immediately obvious.

and,

$$\frac{\partial p_1}{\partial u_a}\bigg|_{u_{r1}} = \frac{\dfrac{k_1}{p_1}}{\left(\dfrac{k_1}{p_1^2} \cdot (u_a - 1) + \dfrac{K_0 v_0^2}{(K_0 \cdot v_0 + p_1)^2} + \dfrac{1}{K_{rc}}\right)} \qquad (22)$$

Similarly, for the axial pull force [equation (12)]

$$dF_a = \frac{\partial F_a}{\partial p_1}\bigg|_{u_a} \cdot dp_1 + \frac{\partial F_a}{\partial u_a}\bigg|_{p_1} \cdot du_a \qquad (23)$$

where

$$\frac{\partial F_a}{\partial p_1}\bigg|_{u_a} = A_1 \tan \phi' \qquad (24)$$

and,

$$\frac{\partial F_a}{\partial u_a}\bigg|_{p_1} = \frac{4\pi^2 L_f C}{l^2 (u_a + L_r)^2} \qquad (25)$$

Substituting dp_1 from equation (20) into (23), and rearranging gives;

$$\frac{\partial F_a}{\partial u_{r1}}\bigg|_{u_a} = \frac{\partial F_a}{\partial p_1}\bigg|_{u_a} \cdot \frac{\partial p_1}{\partial u_{r1}}\bigg|_{u_a} \qquad (26)$$

$$\frac{\partial F_a}{\partial u_a}\bigg|_{u_{r1}} = \frac{\partial F_a}{\partial p_1}\bigg|_{u_a} \cdot \frac{\partial p_1}{\partial u_a}\bigg|_{u_{r1}} + \frac{\partial F_a}{\partial u_a}\bigg|_{p_1} \qquad (27)$$

Combining equations (21), (22), (26) and (27) a differential formulation for the deformability of the cable joint interface during bond failure is obtained;

$$\begin{bmatrix} dF_a \\ dp_1 \end{bmatrix} = \begin{bmatrix} K_1^i & K_2^i \\ K_3^i & K_4^i \end{bmatrix} \begin{bmatrix} du_{r1} \\ du_a \end{bmatrix} \qquad (28)$$

The matrix represents the tangent stiffness matrix for the cable–grout interface and is in general asymmetric.

The Grout Annulus

Assuming that the cement annulus has fully split after 1 mm of axial pull (i.e. at the end of stage 2), it will thereafter be unable to support a tensile tangential stress. Furthermore, the radial fractures will be free to open or close, so that three possible states can be defined (Fig. 22) depending on:

(i) the magnitude p_2 applied to the outer surface of the grout annulus
(ii) the dilation induced by failure at the cable–grout interface (u_{r1}).

The former will act to close the radial fractures, so forcing the annulus to behave more like a thick walled hollow cylinder, whereas the latter will jack them apart so causing the annulus to behave as a series of independent wedges. Incrementally, this behaviour can be written:

$$dp_1 = \frac{\partial p_1}{\partial p_2}\bigg|_{u_{r1}} \cdot dp_2 + \frac{\partial p_1}{\partial u_{r1}}\bigg|_{p_2} \cdot du_{r1} \qquad (29)$$

where p_2 and u_{r1} have been designated as the independent (i.e. control) variables. The corresponding changes in the radial dilation measured at the outside of the annulus are:

$$du_{r2} = \frac{\partial u_{r2}}{\partial p_2}\bigg|_{u_{r1}} \cdot dp_2 + \frac{\partial u_{r2}}{\partial u_{r1}}\bigg|_{p_2} \cdot du_{r1} \qquad (30)$$

CASE 1 Fractures tightly closed

$(r_c = r_1)$

CASE 2 Fractures partially closed

$(r_1 < r_c < r_2)$

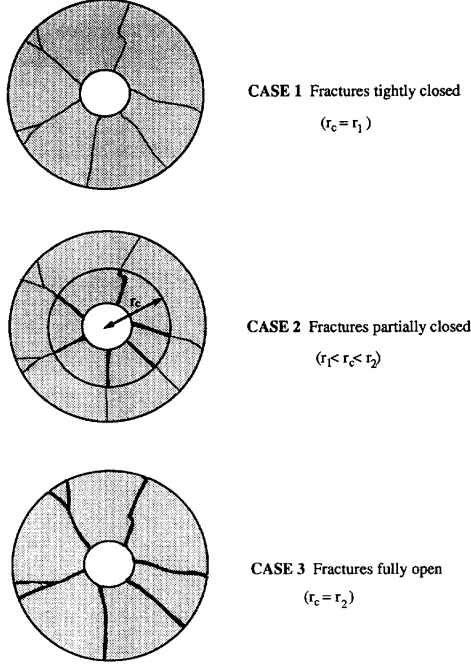CASE 3 Fractures fully open

$(r_c = r_2)$

Fig. 22. The three possible states for the cement annulus: case 1, fractures tightly closed; case 2, fractures partially open; case 3, fractures fully open.

The form of the partial derivatives is dependent on the state of the fractured cement annulus. Since they are more easily derived, the two end member cases will be discussed and then the intermediate case.

Case 1: $(r_c = r_1)$ radial fractures are closed

Although, fully fractured, it will be assumed that the grout annulus will behave identically to an intact hollow cylinder while the tangential stresses are compressive. Thus, using the plane strain elastic solution for a thick wall hollow cylinder [35]:

$$p_1 = \frac{E_g(r_2^2 - r_1^2)u_{r1}}{(1 + v_g)r_1((1 - 2v_g)r_1^2 + r_2^2)} + \frac{2(1 - v_g)r_1^2 p_2}{(1 - 2v_g)r_1^2 + r_2^2} \quad (31)$$

$$u_{r2} = \frac{2(1 - v_g)r_1 r_2 u_{r1}}{(1 - 2v_g)r_1^2 + r_2^2} + \frac{r_2(1 + v_g)}{E_g(r_2^2 - r_1^2)}$$

$$\times \left\{ \frac{4(1 - v_g)^2 r_1^2 r_2^2}{(1 - 2v_g)r_1^2 + r_2^2} - [(1 - 2v_g)r_2^2 + r_1^2] \right\} p_2 \quad (32)$$

Differentiating (31) and (32):

$$\left. \frac{\partial p_1}{\partial p_2} \right|_{u_{r1}} = \frac{2(1 - v_g)r_2^2}{(1 - 2v_g)r_1^2 + r_2^2} \quad (33)$$

$$\left. \frac{\partial p_1}{\partial u_{r1}} \right|_{p_2} = \frac{E_g(r_2^2 - r_1^2)}{(1 + v_g)r_1((1 - 2v_g)r_1^2 + r_2^2)} \quad (34)$$

$$\left. \frac{\partial u_{r2}}{\partial p_2} \right|_{u_{r1}} = \frac{r_2(1 + v_g)}{E_g(r_2^2 - r_1^2)} \left\{ \frac{4(1 - v_g)^2 r_1^2 r_2^2}{(1 - 2v_g)r_1^2 + r_2^2} \right.$$

$$\left. - [(1 - 2v_g)r_2^2 + r_1^2] \right\} \quad (35)$$

$$\left. \frac{\partial u_{r2}}{\partial u_{r1}} \right|_{p_2} = \frac{2(1 - v_g)r_1 r_2}{(1 - 2v_g)r_1^2 + r_2^2} \quad (36)$$

and, the four coefficients in (29) and (30) are obtained.

Case 3: $(r_c = r_2)$ radial fractures are fully open

As described previously by Tepfers [16], Ladanyi [36] and Yazici and Kaiser [31], for the case when the radial fractures are fully open, the geometry reverts from a thick walled hollow cylinder to a series of individual grout wedges (Fig. 22). As outlined in [31], the solution to the stresses for this problem gives:

$$p_1 = p_2 \frac{r_2}{r_1}, \quad (37)$$

which describes a simple force balance between the stress at the inner surface and outer surface of the wedge. As explained by Yazici and Kaiser [31], although the corresponding displacements are unbounded, the deformation of the wedge $(u_{r1} - u_{r2})$ can be determined. Rearranging this result gives:

$$u_{r2} = u_{r1} - \frac{(1 - v_g^2)r_2 \ln\left(\frac{r_2}{r_1}\right)}{E_g} p_2 \quad (38)$$

From (37) and (38), the partial derivatives in equations (29) and (30) can be written as:

$$\frac{dp_1}{dp_2} = \frac{r_2}{r_1} \quad (39)$$

$$\left. \frac{\partial p_1}{\partial u_{r1}} \right|_{p2} = 0 \quad (40)$$

$$\left. \frac{\partial u_{r2}}{\partial p_2} \right|_{u_{r1}} = \frac{(1 - v_g^2)r_2 \ln\left(\frac{r_2}{r_1}\right)}{E_g} \quad (41)$$

$$\left. \frac{\partial u_{r2}}{\partial u_{r1}} \right|_{p2} = 1 \quad (42)$$

and again the required coefficients are obtained.

Case 2: $(r_1 < r_c < r_2)$ radial fractures are partially open

Considering next the transitional case. From equation (34), for an annulus with radial fractures which are tightly closed (case 1), an increase in u_{r1} will cause an increase in p_1. Simultaneously the compressive hoop stress in the annulus will decrease according to:

$$\sigma_\theta = \frac{p_2 r_2^2 - p_1 r_1^2}{r_2^2 - r_1^2} + \frac{(p_1 - p_2)r_1^2 r_2^2}{r^2(r_2^2 - r_1^2)} \quad (43)$$

As explained above, for the radial fractures to be closed $\sigma_\theta > 0$. Thus setting $\sigma_\theta = 0$ in (43), a limit for p_1 can be defined

$$p_1 = \frac{2r_1^2}{r_1^2 + r_2^2} p_2 \quad (44)$$

If p_1 exceeds this, r_c will increase as the cement wedges are pushed apart until $r_c = r_2$ when

$$p_1 = \frac{r_2}{r_1} p_2 \qquad (45)$$

and the annulus is fully open. So, for p_1 within the range:

$$\frac{2r_2^2}{r_1^2 + r_2^2} p_2 < p_1 < \frac{r_2}{r_1} p_2 \qquad (46)$$

the grout annulus consists of an inner ring behaving as a series of independent wedges for which:

$$p_c = \frac{r_1}{r_c} p_1 \qquad (47)$$

and an outer ring for which:

$$p_c = \frac{E_g(r_2^2 - r_c^2)u_{rc}}{(1 + v_g)r_c((1 - 2v_g)r_c^2 + r_2^2)} + \frac{2(1 - v_g)r_2^2 p_2}{(1 - 2v_g)r_c^2 + r_2^2} \qquad (48)$$

The tangential stress in the outer ring $(r_c < r < r_2)$ may be written:

$$\sigma_\theta = \frac{p_2 r_2^2 - p_c r_c^2}{r_2^2 - r_c^2} + \frac{(p_c - p_2)r_c^2 r_2^2}{r^2(r_2^2 - r_c^2)} \qquad (49)$$

Setting $\sigma_\theta = 0$ at $r = r_c$ in (49) and using equation (47), a quadratic in r_c is obtained:

$$G = p_1 r_1 r_c^2 - 2p_2 r_2^2 r_c + p_1 r_1 r_2^2 = 0 \qquad (50)$$

Solving for r_c and taking the root within the range $(r_1 < r_c < r_2)$ gives

$$r_c = \frac{p_2 r_2^2 - r_2\sqrt{p_2^2 r_2^2 - p_1^2 r_1^2}}{r_1 p_1} \qquad (51)$$

Consider next the displacements. For the inner ring, replacing u_{r2} with u_{rc} and r_2 with r_c in equation (38), and using equation (47):

$$u_{rc} = u_{r1} - \frac{(1 - v_g^2)r_1 \ln\left(\dfrac{r_c}{r_1}\right)}{E_g} p_1 \qquad (52)$$

For the outer ring, using thick wall cylinder theory [35] to write u_{rc} in terms of p_c and p_2, and replacing p_c using (47):

$$u_{rc} = \frac{(1 + v_g)r_1}{E_g} \left\{ \frac{(1 - 2v_g)r_c^2 + r_2^2}{r_2^2 - r_c^2} \right\} p_1 - \frac{2(1 - v_g^2)r_c r_2^2}{E_g(r_2^2 - r_c^2)} p_2 \qquad (53)$$

Equating these gives

$$F = u_{r1} - \frac{(1 + v_g)r_1}{E_g} \left\{ \frac{(1 - 2v_g)r_c^2 + r_2^2}{r_2^2 - r_c^2} + (1 - v_g) \right.$$
$$\left. \times \ln\left(\frac{r_c}{r_1}\right) \right\} p_1 + \frac{2(1 - v_g^2)r_c r_2^2}{E_g(r_2^2 - r_c^2)} p_2 = 0 \qquad (54)$$

Next, replacing u_{r1} with u_{rc} and r_1 with r_c in equation (32) we have:

$$u_{r2} = \frac{2(1 - v_g)r_c r_2}{(1 - 2v_g)r_c^2 + r_2^2} u_{rc} + \frac{r_2(1 + v_g)}{E_g(r_2^2 - r_c^2)}$$
$$\times \left\{ \frac{4(1 - v_g)^2 r_c^2 r_2^2}{(1 - 2v_g)r_c^2 + r_2^2} - [(1 - 2v_g)r_2^2 + r_c^2] \right\} p_2 \qquad (55)$$

which gives the displacement at the outside of the cement annulus. Replacing u_{rc} using (52) yields:

$$H = u_{r2} - \frac{2(1 - v_g)r_c r_2}{(1 - 2v_g)r_c^2 + r_2^2} u_{r1} + \frac{2(1 - v_g)(1 - v_g^2)r_c r_2 r_1}{E_g[(1 - 2v_g)r_c^2 + r_2^2]}$$
$$\times \ln\left(\frac{r_c}{r_1}\right) p_1 - \frac{r_2(1 + v_g)}{E_g(r_2^2 - r_c^2)} \left\{ \frac{4(1 - v_g)^2 r_c^2 r_2^2}{(1 - 2v_g)r_c^2 + r_2^2} \right.$$
$$\left. - [(1 - 2v_g)r_2^2 + r_c^2] \right\} p_2 = 0 \qquad (56)$$

Now, functions F, G and H define the three dependent variables (u_{r2}, p_2 and r_c) as implicit functions of the two assigned independent variables (u_{r1} and p_2). From these, using the method of Jacobians, the partial derivatives required for (29) and (30) can be written as the following third-order determinants:

$$\frac{\partial p_1}{\partial p_2}\bigg|_{u_{r1}} = \frac{\dfrac{\partial(F, G, H)}{\partial(u_{r2}, p_2, r_c)}}{\dfrac{\partial(F, G, H)}{\partial(u_{r2}, p_1, r_c)}} \qquad (57)$$

$$\frac{\partial p_1}{\partial u_{r1}}\bigg|_{p2} = \frac{\dfrac{\partial(F, G, H)}{\partial(u_{r2}, u_{r1}, r_c)}}{\dfrac{\partial(F, G, H)}{\partial(u_{r2}, p_1, r_c)}} \qquad (58)$$

$$\frac{\partial u_{r2}}{\partial p_2}\bigg|_{u_{r1}} = \frac{\dfrac{\partial(F, G, H)}{\partial(p_1, p_2, r_c)}}{\dfrac{\partial(F, G, H)}{\partial(p_1, u_{r2}, r_c)}} \qquad (59)$$

$$\frac{\partial u_{r2}}{\partial u_{r1}}\bigg|_{p2} = \frac{\dfrac{\partial(F, G, H)}{\partial(p_1, u_{r1}, r_c)}}{\dfrac{\partial(F, G, H)}{\partial(p_1, u_{r2}, r_c)}} \qquad (60)$$

where

$$\frac{\partial(F, G, H)}{\partial(u_{r2}, p_2, r_c)} = \begin{vmatrix} \dfrac{\partial F}{\partial u_{r2}} & \dfrac{\partial F}{\partial p_2} & \dfrac{\partial F}{\partial r_c} \\ \dfrac{\partial G}{\partial u_{r2}} & \dfrac{\partial G}{\partial p_2} & \dfrac{\partial G}{\partial r_c} \\ \dfrac{\partial H}{\partial u_{r2}} & \dfrac{\partial H}{\partial p_2} & \dfrac{\partial H}{\partial r_c} \end{vmatrix} \text{etc.} \qquad (61)$$

The necessary partial derivatives are evaluated in the Appendix.

Thereby, the coefficients for equations (29) and (30) have been determined for all three cases. Concerning these, several points are of interest:

(i) dp_1/dp_2 calculated from equation (39) (case 3) is greater than that calculated from equation (33) (case 1), while that from equation (57) (case 2) is intermediate. Thus for the same p_2 more stress will be transferred through the grout annulus in the case where the radial fractures are open

(ii) for case 3, $\partial p_1/\partial u_{r1} = 0$, and hence the incremental change in p_1 is only dependent on the
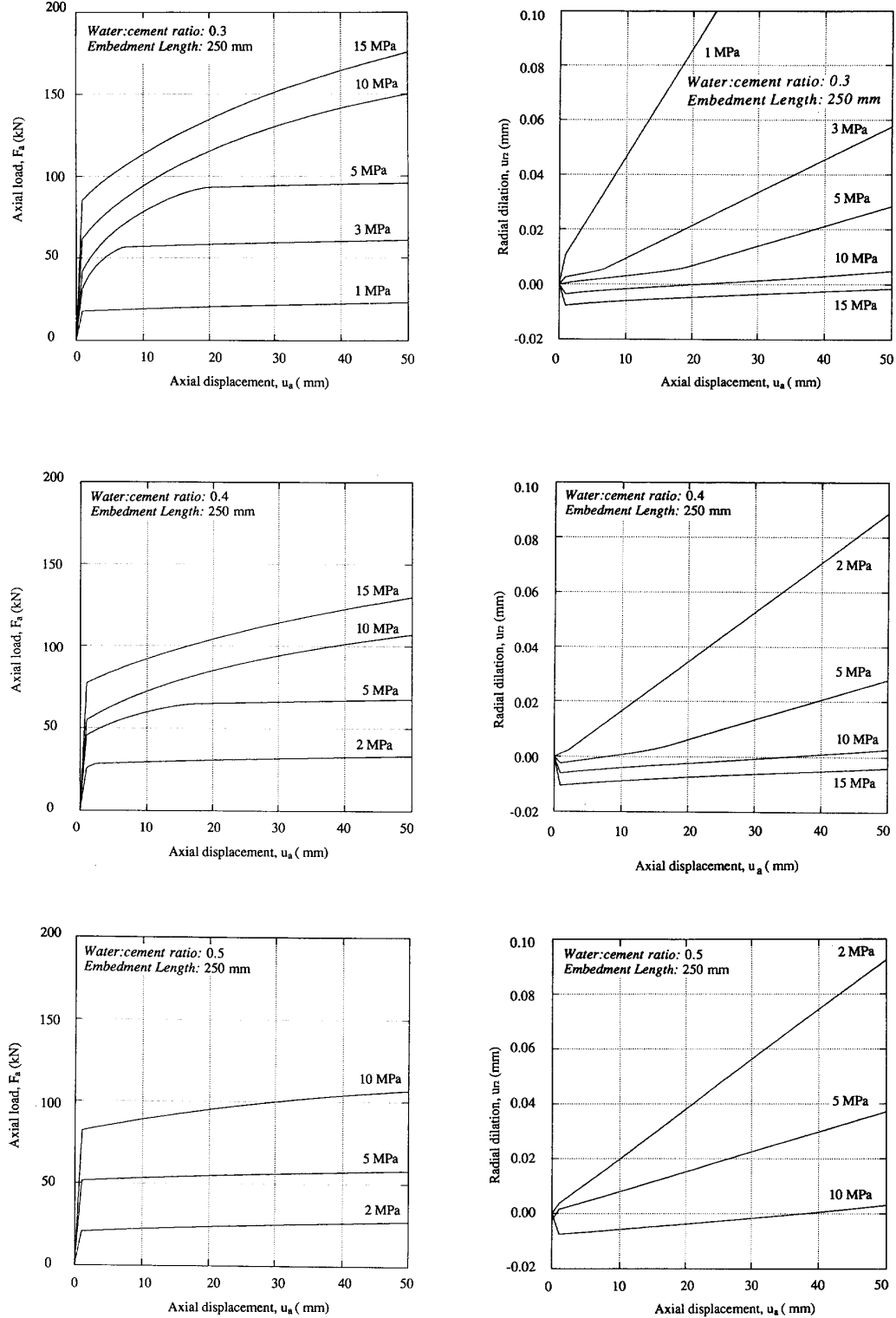
Fig. 23. Simulation of the MHC results using the mathematical model: top, 0.3 w:c ratio; middle, 0.4 w:c ratio; bottom, 0.5 w:c ratio; left, pull force (F_a) vs axial displacement (u_a); right, radial displacement (u_{r2}) vs axial displacement (u_a).

Table 3. Model parameters for the pull test simulations in Fig. 23. Note that only ϕ', E_g and ϵ change

w:c ratio	v_0 (mm)	K_0 (MPa/mm)	k_1 (MPa)	ϕ'	E_g (GPa)	v_g	ϵ ($\mu\epsilon$)
0.30	0.035	30	0.012	23	18.6	0.2	0
0.40	0.035	30	0.012	18	12.1	0.2	400
0.50	0.035	30	0.012	15	9.3	0.2	1500

incremental change in p_2, i.e. it is independent on any radial dilation that occurs. In this case, for p_2 maintained constant (i.e. as during the MHC tests), p_1 must also remain constant. For cases 2 and 3, $\partial p_1/\partial u_{r1} > 0$, so even for p_2 maintained constant during a test, p_1 must increase with dilation

(iii) according to equations (36) and (60), for cases 1 and 2 $\partial u_{r2}/\partial u_{r1}$ is always less than 1, in other words some of the dilation induced at the cable–grout interface must be, in effect absorbed by the grout annulus: for case 3, as long as p_2 is maintained constant, the grout wedges will not deform and hence $\partial u_{r2}/\partial u_{r1} = 1$ and the deformations at the inside and outside of the annulus are equal.

Coupling of the Cable–Grout Interface to the Grout Annulus

The stiffness relations for the cable–grout interface given by equations (19) and (23) may be written:

$$\begin{aligned} \frac{dF_a}{dp_1} = \begin{bmatrix} K_1^i & K_2^i \\ K_3^i & K_4^i \end{bmatrix} \begin{matrix} du_{r1} \\ du_a \end{matrix} \end{aligned} \qquad (62)$$

Likewise, equations (29) and (30), which represent the incremental behaviour of the cement annulus presuming that p_2 and u_{r1} are the independent variables may be written as†:

$$\begin{aligned} \frac{dp_1}{du_{r2}} = \begin{bmatrix} K_1^a & K_2^a \\ K_3^a & K_4^a \end{bmatrix} \begin{matrix} dp_2 \\ du_{r1} \end{matrix} \end{aligned} \qquad (63)$$

du_{r1} and dp_1 are common to both sets of equations and at the inner surface of the grout annulus must be equal. Thus substitution gives:

$$dF_a = \frac{K_1^i \cdot K_1^a}{(K_3^i - K_2^a)} \cdot dp_2$$

$$+ \frac{K_2^i \cdot K_3^i - K_2^i \cdot K_2^a - K_4^i \cdot K_1^i}{(K_3^i - K_2^a)} \cdot du_a \qquad (64)$$

and,

$$du_{r2} = \frac{K_3^a \cdot K_3^i + K_1^a \cdot K_4^a - K_2^a \cdot K_3^a}{(K_3^i - K_2^a)} \cdot dp_2$$

$$+ \frac{K_4^a \cdot K_4^i}{(K_3^i - K_2^a)} \cdot du_a \qquad (65)$$

or in matrix form:

$$\begin{aligned} \frac{dF_a}{du_{r2}} = \begin{bmatrix} K_1 & K_2 \\ K_3 & K_4 \end{bmatrix} \begin{matrix} dp_2 \\ du_a \end{matrix} \end{aligned} \qquad (66)$$

†The matrix is not a stiffness matrix but a matrix which relates the independent variables to the dependent variables. It can be rearranged to give a stiffness matrix.

which fully describes the incremental behaviour of bond failure during an MHC test. Notice that p_2, the pressure maintained in the MHC, and u_a, the displacement applied to the cable by the testing machine, are independent (i.e. control) variables: F_a, the pull force, and u_{r2}, the radial dilation measured at the outer surface of the cement annulus by the cantilever strain gauge arms in the MHC, are dependent variables.

Using equation (66) the pull test results presented above can be simulated. Figure 23 shows the calculated $F_a - u_a$ and $u_{r2} - u_a$ responses for tests conducted at constant confining pressures, for 0.3, 0.4 and 0.5 w:c ratio grouts. The parameters for grout annulus are listed in Table 3. The empirical cable–grout interface parameters (ϕ', K_0, k_1) have been determined using a best fit to the MHC data at $u_a = 1$ mm and $u_a = 50$ mm. In between, the shape of the pull curves is controlled by the analytical solution to the incremental behaviour of the fractured cement annulus as the wedges are forced apart by dilation at the cable–grout interface. Comparing Fig. 23 with Fig. 6, the agreement is relatively good.

Figure 24 shows how r_c varies for the 0.3 tests. Notice that:

(i) for 1 MPa the annulus if forced open ($r_c = r_2$) as soon as it splits and hence according to equation (31), because p_2 is maintained constant, p_1 remains constant and the only increase in F_a is related to the work done in untwisting the free length of cable
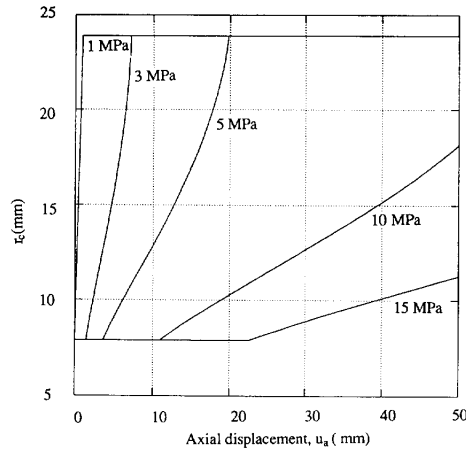

Fig. 24. r_c vs u_a using the mathematical simulation of the MHC cable pull tests for 0.3 w:c ratio. For $p_2 = 1$ MPa the annulus is fully open after splitting; for $p_2 = 3$ and 5 MPa it opens fully during the pull test; for $p_2 = 10$ and 15 MPa it remains partially closed after 50 mm of axial displacement.
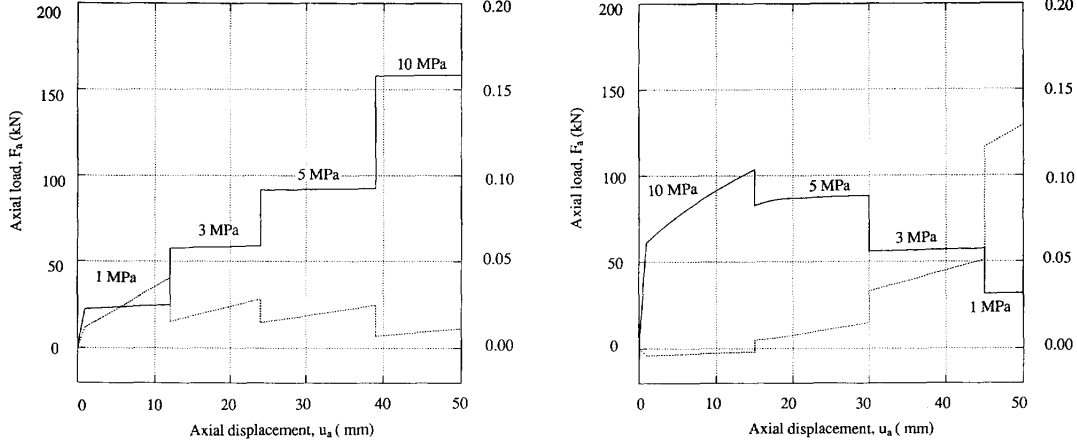
Fig. 25. Simulation using the mathematical model of the MHC cable pull tests under variable radial confining pressure (p_2).
See Fig. 17 for comparison.

(ii) for 3 and 5 MPa the annulus is initially closed ($r_c = r_1$) but is progressively forced open until fully open at 7 and 20 mm respectively. During the process p_1 increases and the pull curve progressively rolls over

(iii) for 10 and 15 MPa the dilation at the cable–grout interface is insufficient to fully open the annulus during the pull test. Hence the load–displacement curves do not roll over completely, and after 50 mm of axial pull $p_1 < p_2 \cdot r_2/r_1$ and the increase in pullout capacity (F_p), which depends on confining pressure, is less. This effect also accounts for the non-linearity in Q2 of Fig. 13.

The pull test simulations for 0.4 and 0.5 w:c ratios, which are also shown in Fig. 23, indicate that the model is able to account for changes in grout quality. Its ability to simulate cable bolt failure under different boundary conditions will be evaluated next.

Cable bolt failure under variable radial confining pressure

Figure 25 shows the model simulation of the tests for which the confining pressure was varied. The cable system parameters are identical to those listed in Table 3 for a 0.3 w:c ratio grout. The results are essentially identical to those obtained using the graphical method (Fig. 17) and show a reasonably good agreement with the limited experimental data (Fig. 15). However, as with the graphical method, reservations exist concerning the modelling of path dependent effects.

Coupling to the Borehole Wall

Assuming a linear material, the response of the borehole wall can be written:

$$dp_2 = K_r \cdot du_{r2} \qquad (67)$$

where K_r is the radial stiffness of the borehole wall. For plane strain

$$K_r = \frac{dp_2}{du_{r2}} = \frac{E_r}{(1 + v_r)r_2} \qquad (68)$$

where E_r and v_r are the elastic properties of the rock surrounding the borehole. Combining equations (64) and (67) gives:

$$dF_a = \left(\frac{K_4 K_1 K_r}{(1 - K_3 K_r)} + K_2 \right) du_a \qquad (69)$$

The coefficient is the tangent axial stiffness for bond failure under a condition of constant radial stiffness.

Cable bolt failure under constant radial stiffness

Figure 26 shows model simulations, using equation (69) for values of K_r corresponding to Sch. 80 steel, aluminium and PVC. The cable bolt system parameters are the same as those listed in Table 3 for a 0.3 w:c ratio grout. Comparing the model predictions with
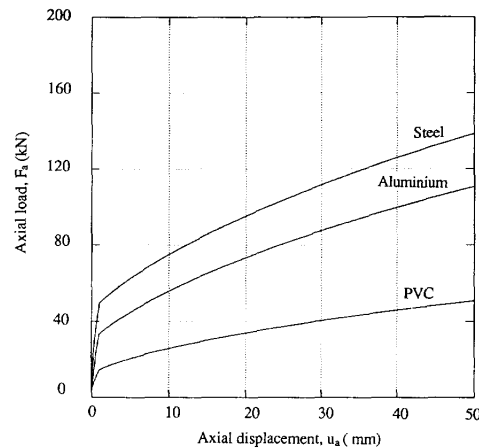

Fig. 26. Simulation using the mathematical model of cable pull test results conducted under constant radial stiffness boundary conditions in steel, aluminium and PVC Pipes.

the experimental results in Fig. 16 indicates a good agreement.

DISCUSSION

Cable pull tests conducted using a modified Hoek cell confirm that cable bolt bond strength is related to frictional rather than adhesional resistance. After 50 mm of axial displacement, the radial dilations measured at the midpoint of the test section are miniscule—decreasing from approx. 0.15 mm for 1 MPa radial confining pressure, to 0.02 mm for 15 MPa. SEM micrographs reveal that shearing of the grout flutes only occurred within 75 mm of the exit point. The only viable explanation is that, along the majority of the test section, failure involves unscrewing of the cable from the cement annulus. This type of failure mechanism is due to the helical form and low torsional rigidity of a seven-wire strand, and it distinguishes the mechanical behaviour of cable bolt bond failure from that of a solid deformed bar.

The data have been used to develop a model for the frictional–dilational behaviour of a fully-grouted cable bolt during bond failure. This has been presented in both graphical and mathematical form. The latter is amenable to implementation into numerical analyses, such as finite element, finite difference and discrete element computer programs. The ability of both models to simulate tests under constant radial confining pressure, tests under constant radial stiffness boundary conditions and tests for which the radial confining pressure was varied has been demonstrated. For the latter, the correlation was only moderate, perhaps because an implicit assumption of the model is that the bond strength is independent of load path. This may not be true, because the contribution of different failure mechanisms is pressure dependent, and hence the amount of unscrewing versus shearing of the cement flutes, and the amount of damage to the grout flutes, will depend on the load path. However, the mathematical model does provide an opportunity, once implemented in a numerical program, to realistically simulate the interaction between the rock mass adjacent to an excavation and an array or pattern of cables designed to reinforce it.

From an operational perspective, the results and observations explain why grouted cable is susceptible to bond failure, and in particular costly dilution due to unravelling, sluffing or peeling of hanging walls. Since the bond strength is frictional, it depends on the pressure generated at the cable–grout interface, which in turn depends on the reaction force generated at the borehole wall caused by dilation during bond failure. For high bond strengths, this dilation is in the order of 20 μm, so that if for any reason:

—less dilation is generated at the cable–grout interface (due to a low torsional rigidity of cables from different manufactures)
—the dilation is absorbed by the grout annulus, either because the grout has a low modulus, has voids or an empty breather tube

—the borehole wall is compliant, perhaps because the wall rock is compliant or fractured, or the immediate wall has been damaged due to drilling or is coated with drill tailings
—the borehole wall relaxes due to mining induced destressing
—some combination of all of the aforementioned

the reaction force will not develop and the resultant bond strength will be low. Since the cable bond strength is sensitive to such small radial dilations and minesite quality control is so difficult to ensure, inconsistent or inadequate cable performance may be unavoidable. In fact, the only consistent feature for instances of failures in cable bolted ground, is that the bond strength mobilized is never sufficient to rupture the cable in tension. Of course, in those instances where the bond strength was higher the ground is less likely to fail, and consequently instances where the cable support system was effective are less apparent. For many mining applications, particularly those related to dilution control in open stoping, the solution to this problem is to force higher radial dilations using modified cable geometries, such as Birdcage, Nutcase or Garford Bulb cable bolts.

REFERENCES

1. Goris J. M. Laboratory evaluation of cable bolt supports. *92nd Annual General Meeting of the CIM*, Ottawa, Canada, May (1990).
2. Reichert R. D., Bawden W. F. and Hyett A. J. Evaluation of design bond strength for fully grouted cable bolts. *Bull. Can. Inst. Min. Metall.* **85**, 110–118 (1992).
3. Desgagnes A. C. An investigation of the mechanics of cable bolt failure. B.Sc. thesis, Queen's University at Kingston, Ontario, Canada (1993).
4. Fuller P. G. and Cox R. H. T. Mechanics of load transfer from steel tendons to cement based grout. *Proc. 5th Aust. Conf. on the Mechanics of Structures and Materials*, Melbourne, pp. 189–203 (1975).
5. Goris J. M. Laboratory evaluation of cable bolt supports. USBM Report of Investigations 9308. (1990).
6. Hyett A. J., Bawden W. F. and Reichert R. D. The effect of rock mass confinement on the bond strength of fully grouted cable bolts. *Int. J. Rock Mech. Min. Sci. & Geomech. Abstr.* **29**, 503–524 (1992).
7. Hassani F. P., Mitri H. S., Khan U. H. and Rajaie H. Experimental and numerical studies of the cable bolt support systems. In *Rock Support in Mining and Underground Construction* (Edited by Kaiser P. K. and McCreath D. R.), pp. 411–417. Balkema, Ontario (1992).
8. Stillborg B. Experimental investigation of steel cables for rock reinforcement in hard rock. Ph.D. thesis, University of Lulea (1984).
9. Rajaie H. Experimental and numerical investigations of cable bolt support systems. Ph.D. thesis, McGill University, Montreal, Canada (1990).
10. Potvin Y., Milne D. and Gendron A. Cable bolt research project—status report. NTC internal report (1989).
11. Bawden W. F., Hyett A. J. and Lausch P. An experimental procedure for the in situ testing of cable bolts. *Int. J. Rock Mech. Min. Sci. & Geomech. Abstr.* **29**, 525–533 (1992).

12. Hoek E. and Franklin J. A. Simple triaxial cell for field or laboratory testing of rock. *Trans. Inst. Min. Metall.* **77**, 22–26 (1968).
13. MacSporran G. R. An empirical investigation into the effects of mine induced stress change on standard cable bolt capacity. M.Sc. thesis, Queen's University, Kingston, Ontario, Canada (1992).
14. Hyett A. J., Bawden W. F. and Coulson A. L. Physical and mechanical properties of normal Portland cement pertaining to fully grouted cable bolts. In *Rock Support in Mining and Underground Construction* (Edited by Kaiser P. K. and McCreath D. R.) (1992).
15. Reichert R. D. A laboratory and field investigation of the major factors influencing the bond capacity of grouted cable bolts. M.Sc. thesis, Queen's University, Kingston, Ontario, Canada (1990).
16. Tepfers R. Cracking of concrete cover along anchored deformed reinforcing bars. *Mag. Concr. Res.* **31**, 3–12 (1976).
17. Bazant Z. P. and Sener S. Size effects in pullout tests. *ACI Mater. Jl* **8**, 347–351 (1988).
18. Lutz L. and Gergely P. Mechanics of bond and slip of deformed bars in concrete. *ACI J.* **64**, 711–720 (1967).
19. Gambrova P. G., Rosati G. P. and Zasso B. Steel-to-concrete bond after concrete splitting: test results. *Mater. Str. RILEM* **22**, 35–47 (1989).
20. Laldji S. and Young A. G. Bond between steel strand and cement grout in ground anchorages. *Mag. Concr. Res.* **40**, 90–98 (1983).
21. Burns S. M. Mechanics of load transfer in cable-reinforced materials. Ph.D. thesis, University of Illinois, Chicago, IL (1992).
22. Tan R. A load–displacement relation for single 7-wire strand cable bolts and its implementation into FLAC and UDEC. Ph.D. thesis, Queen's University, Kingston, Ontario, Canada (1994).
23. Newland P. L. and Allely B. H. Volume changes in drained triaxial tests on granular media. *Geotechnique* **7**, 17–34 (1957).
24. Jaeger J. C. Friction of rocks and stability of rock slopes. *Geotechnique* **21**, 97–134 (1971).
25. Ladanyi B. and Archambault G. Simulation of shear behaviour of a jointed rock mass. *Proc. 11th Symp. on Rock. Mech.*, pp. 105–125 (1970).
26. Goodman R. E. *Methods of Geological Engineering in Discontinuous rock.* West, St Paul, MN (1976).
27. Saeb S. and Amadei B. Modelling rock joints under shear and normal loading *Int. J. Rock Mech. Min. Sci. & Geomech. Abstr.* **29**, 267–278 (1983).
28. Leichnitz W. Mechanical properties of rock joints. *Int. J. Rock Mech. Min. Sci. & Geomech. Abstr.* **22**, 313–322 (1985).
29. Archambault G., Fortin M., Gill D. E., Aubertin M. and Ladanyi B. Experimental investigation of an algorithm simulating the effect of variable normal stiffness on discontinuity shear strength. *Proc. Int. Conf. on Rock Joint*, Loen, Norway, pp. 141–148 (1990).
30. Goodman R. and Boyle W. Non-linear analysis for calculating the support of a b lock with dilatant joint surfaces. Presented at *34th Geomechanics Colloquium*, Salzburg, Austria (1985).
31. Yazici S. and Kaiser P. K. Bond strength of grouted cables. *Int. J. Rock Mech. Min. Sci. & Geomech. Abstr.* **29**, 279–292 (1992).
32. Kaiser P. K., Yazici S. and Nose J. Effect of stress change on the bond strength of fully grouted cables. *Int. J. Rock Mech. Min. Sci. & Geomech. Abstr.* **29**, 293–306 (1992).
33. Chiu H. K. and Dight P. M. Prediction of the performance of rock-socketed side-resistance only piles using profiles. *Int. J. Rock Mech. Min. Sci. & Geomech. Abstr.* **20**, 21–32 (1983).
34. Deiderichs M. S., Pieterse E., Nose J. and Kaiser P. K. A model for evaluating cable bolt bond strength: an update. *EUROCK '93*, Portugal (1993).
35. Popov E. P. *Mechanics of materials.* Prentice-Hall, Englewood Cliffs, NJ (1978).
36. Ladanyi B. A lower bound solution for bursting of thick-walled cylinders of rock under internal and external pressures. *Structures et Comportement Mechanique des Geomateriaux, Colloque Rene Houpert*, Nancy (1992).

APPENDIX

For the function F:

$$F = u_{r1} - \frac{(1 + v_g)r_1}{E_g}\left\{\frac{(1 - 2v_g)r_c^2 + r_2^2}{r_2^2 - r_c^2} + (1 - v_g)\ln\left(\frac{r_c}{r_1}\right)\right\}p_1$$

$$+ \frac{2(1 - v_g^2)r_c r_2^2}{E_g(r_2^2 - r_c^2)}p_2 = 0$$

$$\frac{\partial F}{\partial u_{r2}} = 0$$

$$\frac{\partial F}{\partial p_2} = \frac{2r_c r_2^2(1 - v_g^2)}{E_g(r_2^2 - r_c^2)}$$

$$\frac{\partial F}{\partial r_c} = \frac{-p_1(1 - v_g^2)r_1(r_2^2 + r_c^2)^2}{E_g r_c(r_2^2 - r_c^2)^2} + \frac{2p_2 r_2^2(1 - v_g^2)(r_2^2 + r_c^2)}{E_g(r_2^2 - r_c^2)^2}$$

$$\frac{\partial F}{\partial u_{r1}} = 1$$

$$\frac{\partial F}{\partial p_1} = \frac{-r_1(1 + v_g)}{E_g}\left\{\frac{(1 - 2v_g)r_c^2 + r_2^2}{(r_2^2 - r_c^2)} + (1 - v_g)\ln\left(\frac{r_c}{r_1}\right)\right\}$$

For the function G:

$$G = p_1 r_1 r_c^2 - 2p_2 r_2^2 r_c + p_1 r_1 r_2^2 = 0$$

$$\frac{\partial G}{\partial u_{r2}} = 0$$

$$\frac{\partial G}{\partial p_2} = 2r_c r_2^2$$

$$\frac{\partial G}{\partial r_c} = 2p_2 r_2^2 - 2p_1 r_c r_1$$

$$\frac{\partial G}{\partial u_{r1}} = 0$$

$$\frac{\partial G}{\partial p_1} = -r_1(r_2^2 + r_c^2)$$

For the function H:

$$H = u_{r2} - \frac{2(1 - v_g)r_c r_2}{(1 - 2v_g)r_c^2 + r_2^2}u_{r1} + \frac{2(1 - v_g)(1 - v_g^2)r_c r_2 r_1}{E_g[(1 - 2v_g)r_c^2 + r_2^2]}\ln\left(\frac{r_c}{r_1}\right)p_1$$

$$- \frac{r_2(1 + v_g)}{E_g(r_2^2 - r_c^2)}\left\{\frac{4(1 - v_g)^2 r_c^2 r_2^2}{(1 - 2v_g)r_c^2 + r_2^2} - [(1 - 2v_g)r_2^2 + r_c^2]\right\}p_2 = 0$$

$$\frac{\partial H}{\partial u_{r2}} = 1$$

$$\frac{\partial H}{\partial p_2} = \frac{-r_2(1 + v_g)}{E_g(r_2^2 - r_c^2)}\left\{\frac{4(1 - v_g)^2 r_c^2 r_2^2}{(1 - 2v_g)r_c^2 + r_2^2} - [(1 - 2v_g)r_2^2 + r_c^2]\right\}$$

$$\frac{\partial H}{\partial r_c} = \frac{-2u r_1 r_2(1 - v_g)(r_2^2 - r_c^2(1 - 2v_g))}{X^2} + 2p_1(1 - v_g)$$

$$\times (1 - v_g^2)r_2 r_1 \ln\left(\frac{r_c}{r_1}\right)\frac{(r_2^2 - (1 - 2v_g)r_c^2)}{E_g X^2}$$

$$+ \frac{2p_1(1 - v_g)(1 - v_g^2)r_2 r_1}{E_g X} - \frac{2P_2 r_c r_2(1 + v_g)}{E_g(r_2^2 - r_c^2)^2}$$

$$\times \left\{\frac{4(1 - v_g)^2 r_2^2 r_c^2}{X} - (1 - 2v_g)r_2^2 - r_c^2\right\}$$

$$- \frac{p_2 r_2(1 + v_g)}{E_g(r_2^2 - r_c^2)}\left(\frac{8(1 - v_g)^2 r_c r_2^4}{X^2} - 2r_c\right)$$

in which:

$$X = (1 - 2v_g)r_c^2 + r_2^2$$

$$\frac{\partial H}{\partial u_{r1}} = \frac{-2(1 - v_g)r_c r_2}{(1 - 2v_g)r_c^2 + r_2^2}$$

$$\frac{\partial H}{\partial p_1} = \frac{2(1 - v_g)(1 - v_g^2)r_2 r_1 r_c \ln\left(\frac{r_c}{r_1}\right)}{E_g[(1 - 2v_g)r_c^2 + r_2^2]}$$